Downloaded from orbit.dtu.dk on: Apr 11, 2024

DTU Library

Accelerated 2D Cartesian MRI with an 8-channel local B_0 coil array combined with parallel imaging

Tian, Rui; Uecker, Martin; Davids, Mathias; Thielscher, Axel; Buckenmaier, Kai; Holder, Oliver; Steffen, Theodor; Scheffler, Klaus

Published in:
Magnetic Resonance in Medicine

Link to article, DOI:
10.1002/mrm.29799

Publication date:
2024

Document Version
Publisher's PDF, also known as Version of record

Link back to DTU Orbit

Citation (APA):
Tian, R., Uecker, M., Davids, M., Thielscher, A., Buckenmaier, K., Holder, O., Steffen, T., & Scheffler, K. (2024). Accelerated 2D Cartesian MRI with an 8-channel local B_0 coil array combined with parallel imaging. *Magnetic Resonance in Medicine*, *91*(2), 443-465. https://doi.org/10.1002/mrm.29799

General rights
Copyright and moral rights for the publications made accessible in the public portal are retained by the authors and/or other copyright owners and it is a condition of accessing publications that users recognise and abide by the legal requirements associated with these rights.

- Users may download and print one copy of any publication from the public portal for the purpose of private study or research.
- You may not further distribute the material or use it for any profit-making activity or commercial gain
- You may freely distribute the URL identifying the publication in the public portal

If you believe that this document breaches copyright please contact us providing details, and we will remove access to the work immediately and investigate your claim.

Check for updates

Received: 10 March 2023 | Revised: 26 June 2023 | Accepted: 30 June 2023

DOI: 10.1002/mrm.29799

RESEARCH ARTICLE

Magnetic Resonance in Medicine

Accelerated 2D Cartesian MRI with an 8-channel local B_0 coil array combined with parallel imaging

Rui Tian[1] | Martin Uecker[2,3,4,5] | Mathias Davids[6,7] | Axel Thielscher[8,9] | Kai Buckenmaier[1] | Oliver Holder[1] | Theodor Steffen[1] | Klaus Scheffler[1,10]

[1]High-Field MR center, Max Planck Institute for Biological Cybernetics, Tübingen, Germany

[2]Institute of Biomedical Imaging, Graz University of Technology, Graz, Austria

[3]Institute for Diagnostic and Interventional Radiology, University Medical Center Göttingen, Göttingen, Germany

[4]German Centre for Cardiovascular Research (DZHK), Partner Site Göttingen, Göttingen, Germany

[5]BioTechMed-Graz, Graz, Austria

[6]A. A. Martinos Center for Biomedical Imaging, Department of Radiology, Massachusetts General Hospital, Charlestown, Massachusetts, USA

[7]Harvard Medical School, Boston, Massachusetts, USA

[8]Department of Health Technology, Technical University of Denmark, Kongens Lyngby, Denmark

[9]Danish Research Centre for Magnetic Resonance, Centre for Functional and Diagnostic Imaging and Research, Copenhagen University Hospital Amager and Hvidovre, Hvidovre, Denmark

[10]Department for Biomedical Magnetic Resonance, University of Tübingen, Tübingen, Germany

Correspondence
Rui Tian, High-Field MR center, Max Planck Institute for Biological Cybernetics, Tübingen, Germany.
Email: rui.tian@tuebingen.mpg.de

Funding information
ERC Advanced Grant, Grant/Award Number: No.834940

Abstract

Purpose: In MRI, the magnetization of nuclear spins is spatially encoded with linear gradients and radiofrequency receivers sensitivity profiles to produce images, which inherently leads to a long scan time. Cartesian MRI, as widely adopted for clinical scans, can be accelerated with parallel imaging and rapid magnetic field modulation during signal readout. Here, by using an 8-channel local B_0 coil array, the modulation scheme optimized for sampling efficiency is investigated to speed up 2D Cartesian scans.

Theory and Methods: An 8-channel local B_0 coil array is made to carry sinusoidal currents during signal readout to accelerate 2D Cartesian scans. An MRI sampling theory based on reproducing kernel Hilbert space is exploited to visualize the efficiency of nonlinear encoding in arbitrary sampling duration. A field calibration method using current monitors for local B_0 coils and the ESPIRiT algorithm is proposed to facilitate image reconstruction. Image acceleration with various modulation field shapes, aliasing control, and distinct modulation frequencies are scrutinized to find an optimized modulation scheme. A safety evaluation is conducted. In vivo 2D Cartesian scans are accelerated by the local B_0 coils.

Results: For 2D Cartesian MRI, the optimal modulation field by this local B_0 array converges to a nearly linear gradient field. With the field calibration technique, it accelerates the in vivo scans (i.e., proved safe) by threefold and eightfold free of visible artifacts, without and with SENSE, respectively.

Conclusion: The nonlinear encoding analysis tool, the field calibration method, the safety evaluation procedures, and the in vivo reconstructed scans make significant steps to push MRI speed further with the local B_0 coil array.

KEYWORDS

image acceleration, magnetic field calibration, nonlinear gradient, parallel imaging, reproducing kernel Hilbert Space, wave-CAIPI

This is an open access article under the terms of the Creative Commons Attribution-NonCommercial License, which permits use, distribution and reproduction in any medium, provided the original work is properly cited and is not used for commercial purposes.
© 2023 The Authors. *Magnetic Resonance in Medicine* published by Wiley Periodicals LLC on behalf of International Society for Magnetic Resonance in Medicine.

1 | INTRODUCTION

Typically, MRI scans subjects by spatially encoding the nuclear magnetization with linear magnetic field gradients.[1] This can be mathematically described as sampling the object's representation along a trajectory traversing its Fourier domain, called k-space,[2–4] with the speed limited by the gradient performance under the safety limits.[5] Inevitably, sampling data in such a sequential manner makes MRI scans inherently slow, and therefore, fast MRI acquisitions have drawn long-standing interests since its invention in 1973.

Early fast MRI techniques include novel pulse sequence design and k-space sampling strategy, such as FLASH which exploits short TR with low flip angle,[6] EPI that samples a segment of k-space data within a single shot RF excitation,[7,8] spiral which uses non-Cartesian trajectory for fast k-space readout,[9] and UNFOLD which explores spatiotemporal dimension to increase the frame rate in dynamic MRI.[10] From 1990s, with increasing popularity of the NMR phased array,[11] distinct sensitivity distributions of multiple RF receiver coils were exploited to disentangle aliased pixels given sub-Nyquist sampling,[12–14] as another physical source to spatially localize spins. Since then, parallel imaging became a driving force to further accelerate MRI scans in three spatial and one temporal dimensions.[12–16]

The sampling efficiency by using linear gradients and RF receivers became further optimized, by combining tailored pulse sequences and parallel imaging reconstruction. By traversing the k-space along a zigzag trajectory,[17,18] or shifting the aliasing patterns along the slice or the phase encoding dimensions as CAIPIRINHA (CAIPI),[19,20] parallel imaging reconstruction can be further improved. The reconstruction of these more sophisticated encoded scans became straightforward to implement with the forward model,[13,21] which describes all encoding terms within a linear system. Moreover, such formalism connects MRI reconstruction with the inverse problem, and meanwhile, the progress made in mathematical signal processing, notably the compressed sensing (CS) for under-Nyquist sampling,[22,23] further boosted up MRI sampling speed in certain applications.[24–28]

Consequently, to achieve highly efficient volumetric gradient echo scans, wave-CAIPI[29] was proposed in 2015 as extended from bunched phase encoding[17] in conjunction with CAIPI,[20] and can be optionally combined with CS.[30] This technique samples k-space along an oversampled corkscrew trajectory, which maximizes the k-space (Cartesian) sampling area per unit time and increases the variation of RF sensitivity among mixed pixels to reach a higher acceleration factor. To implement this, sinusoidal currents with phase shifts were applied in gradient coils along the two orthogonal phase encoding dimensions during the gradient echo readout. In the meantime, shim coils driven by sinusoidal currents were also used to accelerate MRI acquisition, which superimposed fast rotary nonlinear gradient fields (here, second order) during signal readout. This technique, called FRONSAC (i.e., Fast rotary nonlinear spatial acquisition),[31] differs from wave-CAIPI in the sense that, it samples k-space with a "stamp"[32] instead of a single point at a time, which can rotate, grow, or shrink when traversing k-space driven by the linear gradients (here, neglecting RF sensitivity modulation).

For decades, although the underlying mechanism for many linear-gradient driven fast acquisition strategies[29,33] became well explained by the existing MRI sampling theory, the second- or third-order[34] magnetic field modulation in FRONSAC, which stems from developments of nonlinear gradient MRI[31,35–45] (i.e., O-space imaging),[40] appeared much less investigated. Therefore, a concept called "Spread spectrum MRI"[46] as a more general technique was proposed in 2019, which aims at accelerating MRI acquisitions based on rapid modulation of localized (rather than global[29,31]) magnetic fields superimposed with the linear gradients, typically using multiple small-size (and, therefore, local) current loops as adapted from multi-coil shim array.[47,48] These local coil channels with independently driven current waveforms can produce more flexible modulation fields in spatial–temporal domain, and therefore, impose more localized spin phase evolution on objects as fingerprints, to disentangle overlapped pixels in reconstruction. This name originated from the "spread spectrum" in telecommunication,[49] in which orthogonal codes modulation on multiple users was exploited to separate signals from users and achieve multiple access. By combining rapid field modulations possibly with diverse nonlinear field shapes,[34,39,40,43] the local B_0 coil array can be a versatile platform to investigate the optimal B_0 field modulations and further speed up MRI scans.

In this paper, with a newly built 8-channel local B_0 coil array, given its geometry allowing a 16-transceive-32-receive RF array[50] to fit in, we perform highly accelerated 2D Cartesian FLASH scans jointly with parallel imaging (here, SENSE)[13,21] in a 9.4 T human MR scanner. A modulation field calibration method based on current monitors in the power amplifier and the ESPIRiT algorithm[51] is proposed to reconstruct scans accelerated by the local B_0 coils. Several sinusoidal modulation waveforms are analyzed and compared with additional noise amplification and approximation error maps analytically computed in time-domain (e.g., k-space). A safety evaluation for our setup is performed to ensure the safety of human subjects during in vivo scans. Finally, reconstruction for ex vivo phantom tests and in vivo scans are performed to validate the encoding efficiency of our

15322594, 2024, 2, Downloaded from https://onlinelibrary.wiley.com/doi/10.1002/mrm.29799 by Danish Technical Knowledge, Wiley Online Library on [19/12/2023]. See the Terms and Conditions (https://onlinelibrary.wiley.com/terms-and-conditions) on Wiley Online Library for rules of use; OA articles are governed by the applicable Creative Commons License

setup, as a significant step for accelerating MRI scans with local B_0 coil array. An early account of the developed methodology was presented in conference abstracts.[52–54]

2 | THEORY

2.1 | System overview

A new local B_0 coil array consisting of 8 square loops, each in 10 cm × 10 cm with 14-turn (~40 μH measured at 10 kHz), is designed and manufactured in-house. A system overview for this local B_0 coil array with 8-channel waveform control is shown in Figure 1, including a system flow diagram with components connections (Figure 1A), a photo of the installed setup (Figure 1B), power amplifier frequency response (Figure 1C), and simulated magnetic field strength by a local B_0 coil (Figure 1D). A more detailed description with photos of all hardware components is available in Data S1.

2.2 | Signal model for local B_0 field modulation

Mathematically, the presence of the locally modulated B_0 magnetic fields results in another spatial–temporal phase evolution term, on the top of the conventional Fourier and RF sensitivity encoding operator for MRI acquisition. Neglecting spin relaxation effects for simplicity, the acquired time-domain continuous signals obtained by the nth RF receiver coil at the time instant t can be written as:

$$S_n(t) = \int c_n(r)\rho(r) \exp\left\{-\sqrt{-1}\left\{k(t)r + \gamma\sum_{\lambda}\left[B_\lambda(r)\int_0^t I_\lambda(\tau)d\tau\right]\right\}\right\}dr, \tag{1}$$

with $k(t) = \gamma\int_0^t g(\tau)d\tau$ as the k-space trajectory term (i.e., in rad/m). γ is the gyromagnetic ratio (i.e., in rad/s/T), r is the spin spatial location, $\rho(r)$ is the object spin density, $c_n(r)$ is the nth RF sensitivity distribution, $g(\tau)$ is the shaped pulse of the linear gradients, $B_\lambda(r)$ is the B_0 field distribution produced by unit current in the λth local B_0 coil, $I_\lambda(\tau)$ is the programmable current waveform in the λth local coil.

In this paper, the data from multiple RF receivers are either reconstructed independently and later combined using the sum-of-squares (SOS) method, or reconstructed by solving the forward model incorporating both RF sensitivity encoding and local coils modulations to achieve an accumulative acceleration factor, which is denoted as "joint reconstruction" in this paper. The RF coils compression is not yet applied to allow a simple examination of the reconstruction quality mainly based on the local B_0 modulations.

When the field modulation in each TR of a 2D line-by-line Cartesian scan remains identical, the image reconstruction and the geometry factor map (G-map) calculation are performed efficiently with a preconditioner of fast Fourier transform (FFT) along the phase-encoded dimensions, similar to wave-CAIPI[29,46] and is derived in Data S1. However, considering arbitrary waveforms in each channel, images are reconstructed by solving the entire encoding matrix in the forward model, with Moore-Penrose pseudoinverse or iterative least squares methods,[55,56] which inevitably demands large memory and long computation time, but is alleviated by computing in the high-performance computing servers. For future work, the matrix size for explicit formulation can also be minimized by applying the Kaczmarz method, namely the algebraic reconstruction technique, which takes only a row of the encoding matrix during one iteration step, and was used in O-space MRI[40] and CT.[57,58]

2.3 | Sampling efficiency of all "spatial encoders" in arbitrary sampling duration

The encoding efficiency of nonlinear gradients, with respect to image-space noise amplification, can be evaluated by analytically computing the G-map[13] with an encoding matrix incorporating all spatial encoding terms. This measures the SNR efficiency over the entire acquisition period (i.e., the entire encoding matrix); however, the amount of k-space signal representation resolved within arbitrary time intervals (i.e., any one or a few rows of the encoding matrix) cannot be quantified.

Specifically, applying the convolution theorem to Eq. (1), the additional phase modulation by nonlinear gradients corresponds to the convolution of its Fourier transform term with the object's k-space representation. Therefore, instead of sampling a single k-space point at a time, the acquisitions become collecting the sum signals contributed by k-space data within a dynamic "stamp",[32] which can change over time according to the nonlinear gradient waveforms. Unfortunately, at arbitrary time instants, the sampling efficiencies by distinct "stamps" corresponding to various nonlinear gradient fields, which parallel imaging acceleration can be optionally combined with, remain difficult to compare quantitatively. Although pixel-wise quantitative analysis[41,43–45,59–62] for both local spatial resolution and SNR can be obtained by evaluating a single (i.e., local k-space trajectory) or all (e.g., pixel noise variance) columns of the entire

15322594, 2024, 2, Downloaded from https://onlinelibrary.wiley.com/doi/10.1002/mrm.29799 by Danish Technical Knowledge, Wiley Online Library on [19/12/2023]. See the Terms and Conditions (https://onlinelibrary.wiley.com/terms-and-conditions) on Wiley Online Library for rules of use; OA articles are governed by the applicable Creative Commons License

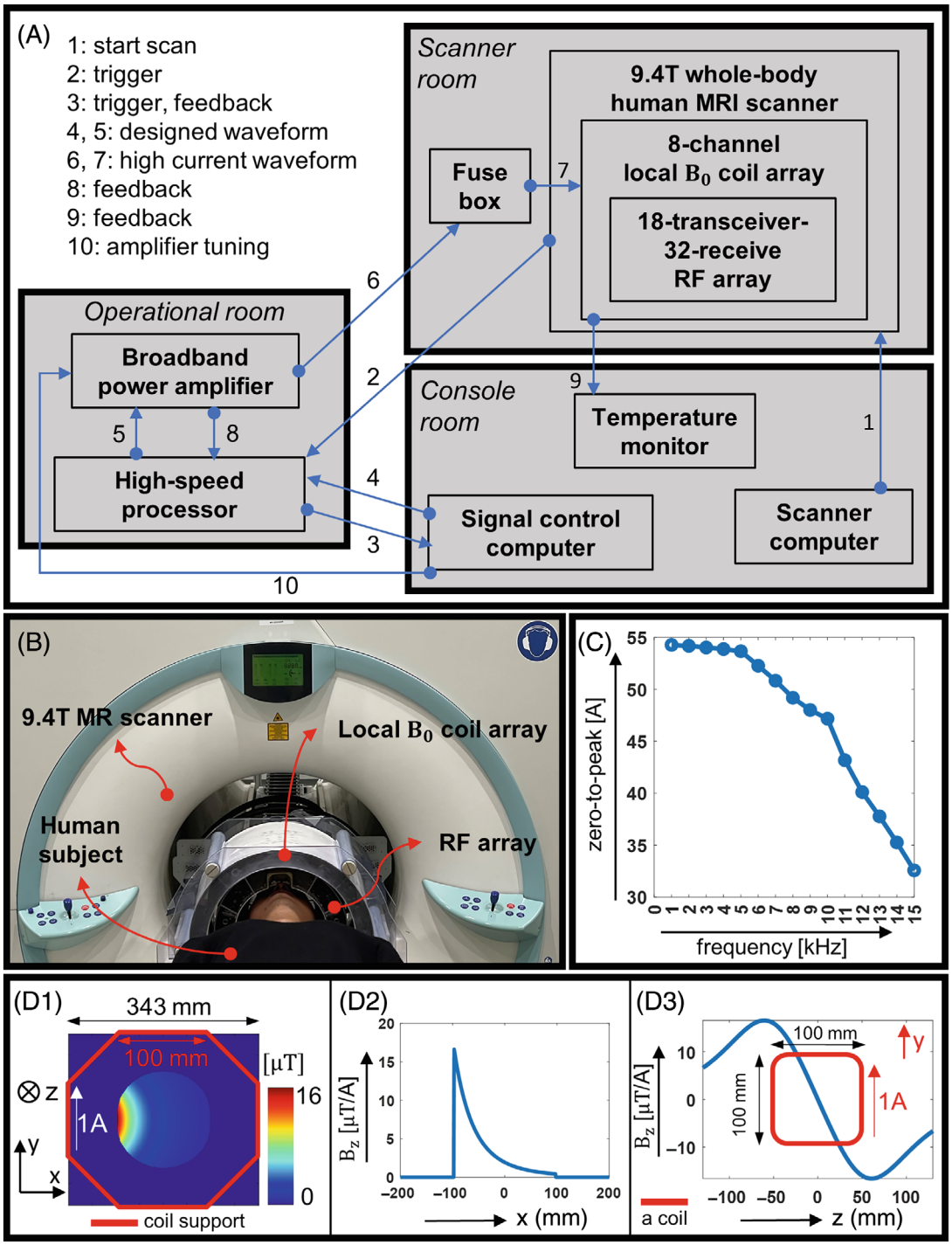

FIGURE 1 System overview. (A) System diagram with the numbered functional flow. The scanner computer starts scans (1), the scanner sends a trigger signal through the high-speed processor to the signal control computer (2, 3), which sends the designed waveforms through the high-speed processor (4) to the broadband power amplifier (5), and outputs high current waveform to the local B_0 coil array (7) protected by the fuse box (6). Simultaneously, the output current is monitored by the power amplifier and recorded through the high-speed processor (8) by the signal control computer (3). The temperature monitor constantly measures the temperature of each local coil during experiments (9), and the signal control computer is used to adjust the tuning setting of the power amplifier once before all experiments. (B) A picture of the installed setup with a human subject. (C) The measured sinusoidal current (zero to peak value) in a frequency ranging from 1 to 15 kHz, output by the broadband power amplifier (averaging between channels). (D1) The simulated magnetic field map given 1A current in a single local B_0 coil. (D2) The 1D plot of the central horizontal line of the map in D1. (D3) The variation of the in-plane maximal field strength generated by 1A in one coil channel (D1) along the z direction, with the relative position to the coil winding.

15222594, 2024, 2, Downloaded from https://onlinelibrary.wiley.com/doi/10.1002/mrm.29799 by Danish Technical Knowledge, Wiley Online Library on [19/12/2023]. See the Terms and Conditions (https://onlinelibrary.wiley.com/terms-and-conditions) on Wiley Online Library for rules of use; OA articles are governed by the applicable Creative Commons License

encoding matrix, how nonlinear gradients at different time points along its "trajectory" (i.e., time integral of gradient waveforms) contributed to the final SNR efficiency of a pixel stays unresolved.

Therefore, in this work, we analytically compute the noise amplification and approximation errors in time-domain (e.g., k-space), to provide more insights over the encoding behavior by the local B_0 coils and guide the waveforms design. To achieve this, a mathematical framework for parallel imaging[63] based on the reproducing kernel Hilbert Space (RKHS) theory is extended by incorporating all spatial encoding terms (e.g., linear and non-linear gradients, RF sensitivity) into the signal model. A simplified version of mathematical derivation is provided below.

Essentially, the image reconstruction can be seen as interpolating the continuous time-domain signal representations of objects from the discrete MRI samples acquired by using all "spatial encoders". The Frobenius norm of the interpolation weights, called the cardinal function, relates to the stability of the interpolation and represents noise amplification as a function of time by the sampling operator. The power function, which yields point-wise bounds of the time-domain approximation error, can also be computed based on this theory.[63]

From the Riesz representation theorem, the MRI spatial encoding can be described by a vector-valued function $\mathbf{K}^{t_{LG},t_{\mathrm{NG}},t_{\mathrm{RF}},i}$ as the representer of evaluation, which includes arbitrary switching of linear,[1,6,7,9] nonlinear gradients[31,43] and RF transmit/receiver coils,[64–72] and maps the compactly supported magnetization image to smooth time-domain acquisition signals. It spans the Hilbert Space H of all signals as a RKHS (i.e., a Hilbert Space of the encoding functions where point-evaluation functionals are continuous), and gives ideal acquired samples $f_i\left(t_{LG}, t_{\mathrm{NG}}, t_{\mathrm{RF}}\right)$ by the inner product evaluation of continuous signal representation f as the reproducing property:

$$f_i\left(t_{LG}, t_{\mathrm{NG}}, t_{\mathrm{RF}}\right) = \left\langle \mathbf{K}^{t_{LG},t_{\mathrm{NG}},t_{\mathrm{RF}},i}, f \right\rangle_{\mathrm{H}}, \tag{2}$$

where $t_{LG}, t_{\mathrm{NG}}, t_{\mathrm{RF}}$ represent the sampling time for linear, nonlinear gradients and RF coils with index i, respectively. Generally, the sampling time for each "spatial encoder" can be written as a separate variable as in Eq. (2), to describe arbitrary and independent controls over distinct encoding elements. In this paper, the RF encoding fields (i.e., only receive) remain fixed over time, and the linear and nonlinear gradients share the same time axis (i.e., switched on simultaneously during signal readout). For this special case, the three independent time dimensions are simplified to one without loss of generality:

$$t = \left(t_{LG}, t_{\mathrm{NG}}, t_{\mathrm{RF}}\right). \tag{3}$$

Next, this RKHS can be uniquely characterized by a kernel function (unnecessarily shift-invariant as in the theory)[63] obtained by applying the forward signal model to the encoding function based on Eq. (1), which captures the similarity of the two argument encoding functions:

$$\begin{aligned}&\mathbf{K}_{ij}\left(t_{LG}, t_{\mathrm{NG}}, t_{\mathrm{RF}}, \bar{t}_{LG}, \bar{t}_{\mathrm{NG}}, \bar{t}_{\mathrm{RF}}\right)\\ &\overset{(3)}{=} \mathbf{K}_{ij}(t,\bar{t}) = \left\langle \epsilon^{t,i}(r), \epsilon^{\bar{t},j}(r)\right\rangle_{\mathrm{L}^2},\end{aligned} \tag{4}$$

$$\begin{aligned}&= \int c_i(r,t)c_j^{\mathrm{H}}(r,\bar{t}) \exp\Bigg\{ -\sqrt{-1}\Bigg\{[k(t)-k(\bar{t})]r\\ &\quad + \gamma\sum_{\lambda} B_\lambda(r)\left[\int_0^t I_\lambda(\tau)d\tau - \int_0^{\bar{t}} I_\lambda(\tau)d\tau\right]\Bigg\}\Bigg\}dr,\end{aligned} \tag{5}$$

where the operator $\langle\cdot,\cdot\rangle$ denotes the inner product, r is the image location, the upper bar for sampling time indicates being for the second kernel argument, $\epsilon^{t,i}(r), \epsilon^{\bar{t},j}(r)$ represent the encoding operator including all "spatial encoders", $c_i(r,t), c_j(r,\bar{t})$ are the RF sensitivity profiles from receiver index i and j (in this paper, constant in time), the operator $(\cdot)^{\mathrm{H}}$ denotes the complex conjugate operation.

Therefore, by defining a measurement subspace $\mathbf{H_S} \subset \mathbf{H}$ spanned by $\mathbf{K}^{\bar{t},j}$, any continuous function $f^{\|} \in \mathrm{H_S}$ can be expressed by linear combination of $\mathbf{K}^{\bar{t},j}$. Further, the discrete MRI samples $f_i^{\|}(\mathrm{t})$ can be obtained by evaluating $f^{\|}$ at the sample locations t, i by building the inner product with the representers of evaluation $\mathbf{K}^{t,i}$, and thus, be expressed by the kernel function:

$$f^{\|} = \sum_{\bar{t},j} a_{\bar{t},j}\mathbf{K}^{\bar{t},j}, \tag{6}$$

where $a_{\bar{t},j}$ is the interpolation coefficient.

$$f_i^{\|}(t) \overset{(2)}{=} \left\langle \mathbf{K}^{t,i}, f^{\|}\right\rangle \tag{7}$$

$$\overset{(4,6)}{=} \sum_{\bar{t},j} a_{\bar{t},j}\mathbf{K}_{ij}(t,\bar{t}) \tag{8}$$

Additionally, because the representers can be used to interpolate all functions in $\mathrm{H_S}$ it spans, theoretically, the acquired time-domain samples can be exactly interpolated to any samples $f_k^{\|}(\dot{t})$ in $\mathrm{H_S}$ evaluated at locations $\dot{t}, k$ by an arbitrary encoding function as a reference (e.g., fully sampled Cartesian k-space encoding), with interpolation weights as the cardinal function $u_k^{t,i}(\dot{t})$:

$$f_k^{\|}(\dot{t}) = \sum_{t,i} f_i^{\|}(t)u_k^{t,i}(\dot{t}), \tag{9}$$

where $\dot{\mathrm{t}}$ and k are the time grid and the RF receiver index of the reference encoding function. Now, the reference

15322594, 2024, 2, Downloaded from https://onlinelibrary.wiley.com/doi/10.1002/mrm.29799 by Danish Technical Knowledge, Wiley Online Library on [19/12/2023]. See the Terms and Conditions (https://onlinelibrary.wiley.com/terms-and-conditions) on Wiley Online Library for rules of use; OA articles are governed by the applicable Creative Commons License

samples $f_k^{\|}(\dot{t})$ can be expressed either directly by kernel $K_{kj}(\dot{t},\bar{t})$, or by kernel encoded acquired samples $f_i^{\|}(t)$ and cardinal function $u_k^{t,i}(\dot{t})$:

$$f_k^{\|}(\dot{t}) \overset{(2)}{=} \left\langle \mathbf{K}^{\dot{t},k}, f^{\|} \right\rangle, \tag{10}$$

$$\overset{(8)}{=} \sum_{\bar{t},j} a_{\bar{t},j} \mathbf{K}_{kj}(\dot{t},\bar{t}), \tag{11}$$

$$\overset{(8,9)}{=} \sum_{t,i,\bar{t},j} a_{\bar{t},j} \mathbf{K}_{ij}(t,\bar{t}) u_k^{t,i}(\dot{t}). \tag{12}$$

Eventually, comparing Eqs. (11) and (12), the cardinal function can be intuitively seen as coefficients, which interpolate the representer of evaluation at arbitrary sampling location of a reference encoding function, exactly from their values at the location of the tested sampling function encoded in kernel:

$$\sum_{t,i} \mathbf{K}_{ij}(t,\bar{t}) u_k^{t,i}(\bar{t}) = \mathbf{K}_{kj}(\dot{t},\bar{t}). \tag{13}$$

Namely, the time-domain noise amplification factor can be obtained by solving a linear system of equations:

$$\mathbf{MU} = \mathbf{R}, \tag{14}$$

$$\text{with} \begin{cases} \mathbf{M} = \mathbf{E}_{\bar{t},j} \mathbf{E}_{t,i}^{*}, \in \mathbb{C}^{TN \times TN} \\ \mathbf{R} = \mathbf{E}_{\bar{t},j} \mathbf{E}_{\dot{t},k}^{*}, \in \mathbb{C}^{TN \times \dot{T}\dot{N}} \end{cases} \tag{15}$$

where $\mathbf{E}_{t,i}$, $\mathbf{E}_{\bar{t},j}$ are both the tested encoding matrix, and $\mathbf{E}_{\dot{t},k}$ is a reference encoding matrix, for evaluating the kernel. The T, N are the total sampling time points and number of RF receivers, with the upper dot indicating being for the reference matrix. The noise amplification factor is obtained by taking the Frobenius norm of U along the dimension of t,i (i.e., taking square for each element in U, summing along the vertical dimension, and taking the square root). The asterisk (*) denotes the conjugate transpose operation.

Furthermore, the time-domain approximation error caused by interpolation can be computed with the power function P in the RKHS theory[63]:

$$\mathbf{P}^{\dot{t},k} = \sqrt{\left(\mathbf{E}_{\dot{t},k} \mathbf{E}_{\dot{t},k}^{*} - \mathbf{U}^{*} \mathbf{E}_{t,i} \mathbf{E}_{\dot{t},k}^{*} \right)_{\text{diag}}}. \tag{16}$$

Theoretically, the reference encoding matrix $\mathbf{E}_{\dot{t},k}$ can be arbitrarily chosen (e.g., another acceleration factor, spiral, wavelet) to visualize how time-domain acquisition signals gradually lead to the noise amplification and approximation error in the corresponding transform domain. Here, assuming RF receivers' sensitivity constant across the image, the reference is chosen as a fully sampled discrete Fourier transform matrix, to demonstrate errors in k-space relative to a fully sampled 2D Cartesian scan. Note that, the Fourier transform operation links the signal representation, but not the standard deviation of the noise signal, between image- and k-space.

Finally, Eq. (14) can be easier to solve with less/-compressed RF receiver channels or a higher undersampling factor. Faster computation with pseudo-replica simulation[33] or approximation[73] is also worth investigating. Furthermore, limiting the encoding matrix from spanning only a sub-interval (e.g., one TR) of the entire sampling period allows quantifying the contributions of signal encoding during smaller temporal periods in relation to the entire k-space.

2.4 | Calibration of B_0 rapid modulation field

Reconstruction of scans accelerated by local B_0 coils requires additional calibration of the field modulation pattern. The estimation errors in the additional phase evolution imposed by the local B_0 coils can manifest as residue artifacts particularly for high acceleration factors, in a mechanism similar to the SENSE residue artifacts because of calibration errors of RF receivers' sensitivity maps.[51]

Theoretically, the additional imposed magnetic field can be measured with a calibration scan modified from the chemical shift sequence, as in O-space MRI.[40] However, this requires time consuming scans with the entire spatial grid phase encoded, to measure phase evolution resulted from different modulation waveforms, and therefore, does not appear to be the most suitable for testing our setup with various modulation schemes. Additionally, the magnetic field probes, as a third-party monitor, could be used to calibrate the linear gradient insert.[74–76] However, its feasibility to track high-order nonlinear gradient fields[61] by our setup has not been testified yet.

Therefore, a field calibration method based on current monitors of the power amplifier and the ESPIRiT algorithm is proposed to calibrate our setup, with only one calibration scan for all experiments given various modulation waveforms. Essentially, low-resolution field mapping scans are input to the ESPIRiT algorithm,[51] mimicking data from multiple RF receivers, to extrapolate high-resolution (i.e., the resolution for reconstruction) phase maps with robustness to avoid possible errors during highly accelerated scans. Moreover, the 8-channel current monitors are exploited to resolve phase offset maps contributed by unit current in a local B_0 coil and combined with the monitored modulation currents in later experiments to reconstruct images. This calibration pipeline is illustrated in Figure 2, with detailed procedure and error evaluation documented in Data S1. In this paper,

15322594, 2024, 2, Downloaded from https://onlinelibrary.wiley.com/doi/10.1002/mrm.29799 by Danish Technical Knowledge, Wiley Online Library on [19/12/2023]. See the Terms and Conditions (https://onlinelibrary.wiley.com/terms-and-conditions) on Wiley Online Library for rules of use; OA articles are governed by the applicable Creative Commons License

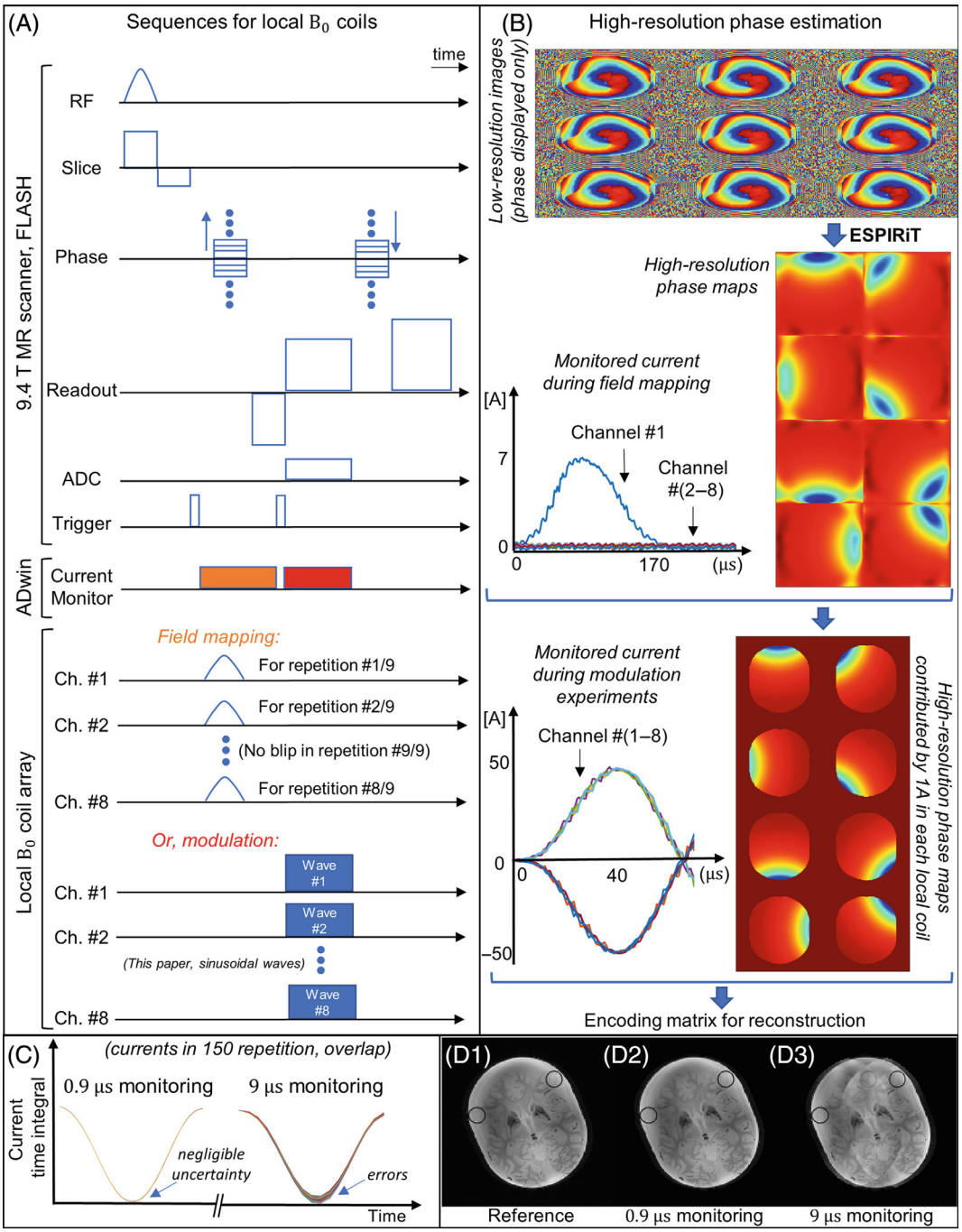

FIGURE 2 Calibration of phase evolution by the local B_0 coil array, with more details for each step and the error evaluation demonstrated in Data S1. (A) The pulse sequences for magnetic field mapping or current modulations of local B_0 coils. (B) Illustration of the phase evolution estimation method, based on low-resolution scans from the sequence shown in (A), current monitors of the power amplifiers, and the ESPIRiT algorithm. Please note that, the low-resolution complex images are displayed only in phase, and the vertical dimension is 40% undersampled in k-space to save scan time. Additionally, the channel coupling between local B_0 coils and linear gradients is included in the monitored currents. (C) The time integral of the current is calculated on an interpolated time grid, based on monitored currents sampled with 0.9 and 9 μs, respectively. Curves of currents from 150 TR are shown with identical linewidth. (D) Reconstruction based on monitored currents with different sampling rates demonstrates the necessity of fast current monitoring for accurate image reconstruction. All these images are reconstructed by inverting the entire encoding matrix in high-performance computing servers, which contains independently monitored currents in each TR without averaging.

15322594, 2024, 2, Downloaded from https://onlinelibrary.wiley.com/doi/10.1002/mrm.29799 by Danish Technical Knowledge, Wiley Online Library on [19/12/2023]. See the Terms and Conditions (https://onlinelibrary.wiley.com/terms-and-conditions) on Wiley Online Library for rules of use; OA articles are governed by the applicable Creative Commons License

given different objects, the field maps for local B_0 coils require recalibration because of variation of the object's support.

2.5 | Optimized sinusoidal modulation for 2D Cartesian sampling

In previous work of spread spectrum MRI,[46] sinusoidal waveforms in 5 kHz, 3A zero-to-peak value, and with $\pi/4$ phase increment between adjacent channels were applied to produce magnetic field modulation and speed up scans. This time, different waveforms are compared for the optimal acceleration of 2D Cartesian scans, with respect to the noise amplification in image-space, and the error maps (i.e., noise amplification and approximation errors) in k-space.

Because the acceleration performance does not solely depend on the additional field modulation schemes, but also the k-space trajectory defined by linear gradients, as a starting point, only 2D line-by-line Cartesian sampling is considered in this paper. Moreover, modulation in more than one single sinusoidal frequency can produce more "wiggling" for k-space trajectory,[77,78] which may provide certain enhancements, but with the underlying mechanism well understood. Therefore, we focus on sinusoidal modulation in only a single frequency for local coils to avoid excessively digressing from scrutinizing characteristics unique to local coils modulations.

2.5.1 | Field shapes—combinations of phase offsets

Sinusoidal currents with distinct combinations of phase offsets are applied to the eight local coil channels and compared. Each scheme leads to a different field patterns oscillating during the readout, including "quadratic," "quadrupolar," and "octupolar" field distributions, a circularly rotated nearly linear gradient field formed by $\pi/4$ phase increment between adjacent coils (denoted as "$\pi/4$"), and a nearly linear gradient field oscillated roughly toward the phase encoding dimension formed by applying phase offset 0 and π for each of the four adjacent coils (denoted as "0&π"). Additionally, a similar phase arrangement of "0&π" is applied in conjunction with a rotation of 22.5° of the linear gradient axis. This allows the nearly linear gradient produced by local coils mostly align along the phase encoding direction, similar to the bunched phase encoding,[17] but with a local gradient setup, and is denoted as "0&π, R22.5°".

The schemes with various phase offset arrangements are defined below (i.e., "scheme": [phase offsets in the eight local B_0 coils]), with the corresponding field/gradient strength distributions and k-space "stamps" calculated from experimentally measured data illustrated in Figure 3. With our array geometry, the "quadratic" scheme produces the strongest magnetic field over the object, the "quadrupolar" produces the maximal gradient field around the edge of FOV, the field produced by the "octupolar" scheme appears much weaker than others, the "0&π" scheme, with or without rotation, provides strong gradient fields across the entire FOV.

- "quadratic": $[0, 0, 0, 0, 0, 0, 0, 0]$
- "quadrupolar": $[0, 0, \pi, \pi, 0, 0, \pi, \pi]$
- "octupolar": $[0, \pi, 0, \pi, 0, \pi, 0, \pi]$
- "$\pi/4$": $[0, \pi/4, \pi/2, 3\pi/4, \pi, 5\pi/4, 3\pi/2, 7\pi/4]$
- "0&π": $[\pi, \pi, 0, 0, 0, 0, \pi, \pi]$
- "0&π, R22.5°": $[\pi, \pi, 0, 0, 0, 0, \pi, \pi]$, with in-plane FOV rotation of 22.5°
- "$\pi/4$, CAIPI": $[0, \pi/4, \pi/2, 3\pi/4, \pi, 5\pi/4, 3\pi/2, 7\pi/4]$, odd steps; $[0, \pi/4, \pi/2, 3\pi/4, \pi, 5\pi/4, 3\pi/2, 7\pi/4] + \pi$, even steps
- "0&π, R22.5°, CAIPI": $[\pi, \pi, 0, 0, 0, 0, \pi, \pi]$, odd steps; $[\pi, \pi, 0, 0, 0, 0, \pi, \pi] + \pi$, even steps (both with 22.5° in-plane FOV rotation).

2.5.2 | Aliasing control—sinusoidal phase shifts between phase-encoded steps

Additional sinusoidal phase offsets can be added in all local B_0 coils between consecutive phase-encoded steps to produce a shifted sampling function for signal readout, as defined in the schemes above as well. Interleaving shifted k-space "stamps" can shift aliasing patterns and reduce noise amplification caused by image acceleration in certain scenarios, similar to CAIPI.[19,20] The reconstruction is performed by inverting the entire encoding matrix, because of the variation of modulation waveforms among TR, in a high-performance computing server for simplicity.

2.5.3 | Frequency selection—k-space coverage for different ranges

Given ~10 kHz cutoff frequency of the power amplifier, a broad range of sinusoidal frequencies is tested to reach optimal accelerations. Considering sinusoidal modulation in a single frequency ω (here, for all local B_0 coils) and phase offset φ_γ, the Eq. (1) can be written as:

$$S_n(t) = \int c_n(r)\rho(r)\exp\{-\sqrt{-1}\{k(t)r + \gamma\sum_\lambda \left[B_\lambda(r)\frac{-\cos(2\pi\omega t + \varphi_\lambda)}{2\pi\omega}\right]\}\}\, dr. \quad (17)$$

15222594, 2024, 2, Downloaded from https://onlinelibrary.wiley.com/doi/10.1002/mrm.29799 by Danish Technical Knowledge, Wiley Online Library on [19/12/2023]. See the Terms and Conditions (https://onlinelibrary.wiley.com/terms-and-conditions) on Wiley Online Library for rules of use; OA articles are governed by the applicable Creative Commons License

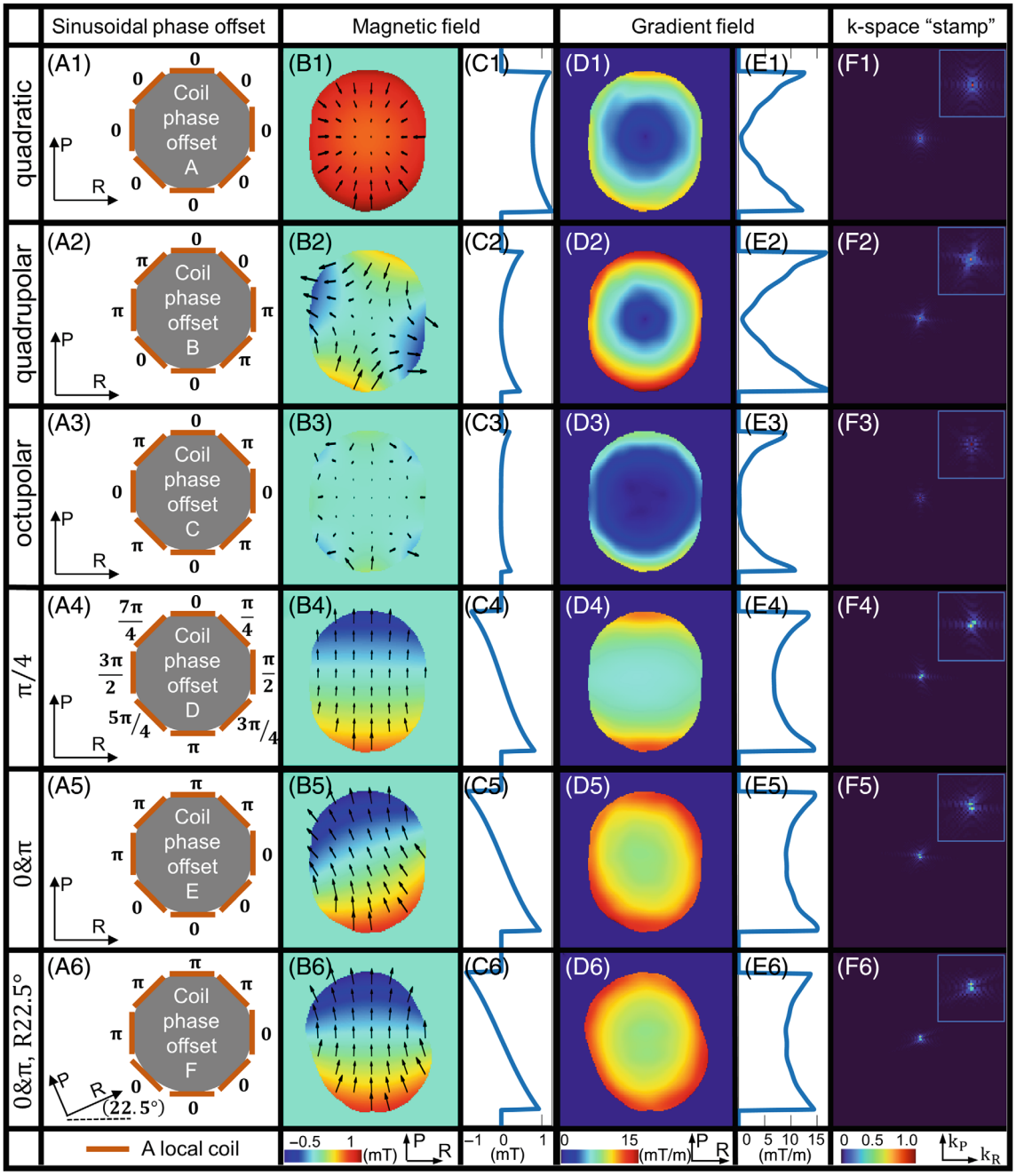

FIGURE 3 The encoding schemes for sinusoidal modulation of local B_0 coils with different phase offset patterns. Rows 1–6: Different sinusoidal phase offset patterns, leading to magnetic field modulation with distinct field shapes. Columns A–F: The 8-channel arrangement for coil phase offset, the 2D magnetic field maps at a time instant during modulation computed from the measured field maps and the coil currents at maximum, the 1D plots along the central vertical line in the 2D magnetic field maps, the 2D gradient field maps at a time instant computed from the measured field maps and the coil currents at maximum, the 1D plots along the central vertical line in the 2D gradient maps, and the 2D k-space "stamps" (absolute value displayed) calculated by taking the Fourier transform of the 2D spatial encoding terms corresponding to the local B_0 coils at current maximum (note, not the maximum of the imposed phase accumulation). The gradient field in columns D and E are calculated as the net local gradient along a single direction in each pixel, namely, the Euclidean norm of the local gradient in the two orthogonal dimensions. Note that, the k-space "stamps" here, only qualitatively show a coarse sampling coverage at a time instant, whereas the cardinal and the power function maps in later sections can quantitatively compute the k-space sampling efficiency in arbitrary acquisition time duration for rigorous comparisons between different "stamps".

15222594, 2024, 2, Downloaded from https://onlinelibrary.wiley.com/doi/10.1002/mrm.29799 by Danish Technical Knowledge, Wiley Online Library on [19/12/2023]. See the Terms and Conditions (https://onlinelibrary.wiley.com/terms-and-conditions) on Wiley Online Library for rules of use; OA articles are governed by the applicable Creative Commons License

Obviously, higher sinusoidal frequency inversely scales the phase evolution as the denominator and leads to narrower k-space sampling coverage along the phase encoding dimension, and the k-space sampling "stamp" should appear more localized. Additionally, the linear gradient bandwidth also plays a role in acceleration efficiency by gradient modulations.[76] In this paper, it is chosen with a scanner analog-to-digital converter dwell time of 3 μs to allow substantial acceleration by modulation, while not causing excessive fat shifts artifacts during in vivo scans in 9.4 T.

3 | METHODS

All experiments are carried out with the 8-channel local B_0 coil array fixed on the patient table of a 9.4 T whole-body human scanner, equipped with gradients (SC72) with maximum slew rate and absolute strength of 200 T/m/s and 70 mT/m, respectively (Siemens Healthineers). A 16-transceive/32-receive RF coil array modified from the reference[50] (here, only circularly polarized [CP] mode used for RF transmission) or a plastic support with field probes (Skope) is inserted inside its support, for imaging or field measurement experiments, respectively.

All imaging experiments are performed with a fully sampled multi-slice 2D FLASH sequence, and undersampled retrospectively to test image acceleration by local coils modulations. The scan sequences are illustrated in Figure 2A. The scan is made with a FOV of 220 mm × 220 mm, and a matrix size of 150 × 150 or 192 × 192 for phantom and in vivo scans, respectively. Sinusoidal currents with 40 A zero-to-peak value (except for 50 A in "field calibration") are used for local B_0 coils to accelerate scans with scanner readout bandwidth (i.e., linear gradients) ~4.5 mT/m. More details about the scan protocols and the information about the ex vivo phantom are documented in Data S1.

4 | RESULTS

4.1 | Phantom experiments with calibrated phase evolution

As shown in Figure 2, the field calibration method described in this paper is used to successfully produce reconstructed images from local B_0 coils modulated scans without additional visible artifacts caused by our setup. In this example, sinusoidal modulation with 7 kHz/50A_{pk} and the phase offset scheme "0&π, R22.5°" are applied. The fully sampled images in Figure 2D are reconstructed by inverting the entire encoding matrix, which is constructed with monitored current signals in all TR with a sampling rate of 0.9 μs or with only a 10-fold undersampled portion (equivalently, sampling at 9 μs). The reconstruction with the fast current monitor sampling rate (i.e., 0.9 μs) has no visible errors compared to the reference image with local coils off, whereas the one with the slower rate has additional aliasing artifacts, because of the estimation errors in currents as shown in Figure 2C. Note that, the coupling effects among all gradients (i.e., local B_0 coils, scanner gradients) are included in the monitored current waveforms, and therefore, do not contribute to reconstruction errors. Typical artifacts taking place when not using the ESPIRiT are demonstrated in Data S1.

4.2 | Sinusoidal modulation with different field shapes

Given multiple RF receivers independently reconstructed and combined using SOS, the phantom tests for 7 kHz/40A_{pk} sinusoidal modulation with distinct phase offset patterns are demonstrated in Figure 4, with respect to the reconstruction with threefold undersampled phase-encoded steps, the G-factor map, and the cardinal and the power function maps given sampling period of a single and all TR, respectively. With our local B_0 array geometry, the scheme "0&π, R22.5°" achieves the best acceleration efficiency for 2D Cartesian MRI, which forms nearly a linear gradient oscillating along phase encoding direction and reduces the mean image-space SNR loss (G-map) by a factor of 3.6 compared to the "π/4" scheme presented in previous work.[46] The images by joint reconstruction of multiple RF receivers and local B_0 modulations show similar tendency and are presented in Figure S5, where the additional encoding by RF receivers' sensitivity does not change the optimal field shape for the 2D Cartesian scan.

For sampling along a straight line in central k-space within one TR, the cardinal function map (column C) generally shows a dark band in the center with high-intensity ripples around its edge and again very dark regions as moving further away. The central dark band corresponds to the sufficiently sampled region by the k-space "stamp," and the bright ripples indicate the noise amplification originated from some signals around the edge of the "stamp", which are contained within the sum signal acquired by the "stamp" but remained inefficiently resolved. The large dark regions at two sides of the central dark band with the bright ripples around are completely untouched by the sampling "stamp", and therefore, no interpolation and the related noise amplification can take place, leading to

15222594, 2024, 2, Downloaded from https://onlinelibrary.wiley.com/doi/10.1002/mrm.29799 by Danish Technical Knowledge, Wiley Online Library on [19/12/2023]. See the Terms and Conditions (https://onlinelibrary.wiley.com/terms-and-conditions) on Wiley Online Library for rules of use; OA articles are governed by the applicable Creative Commons License

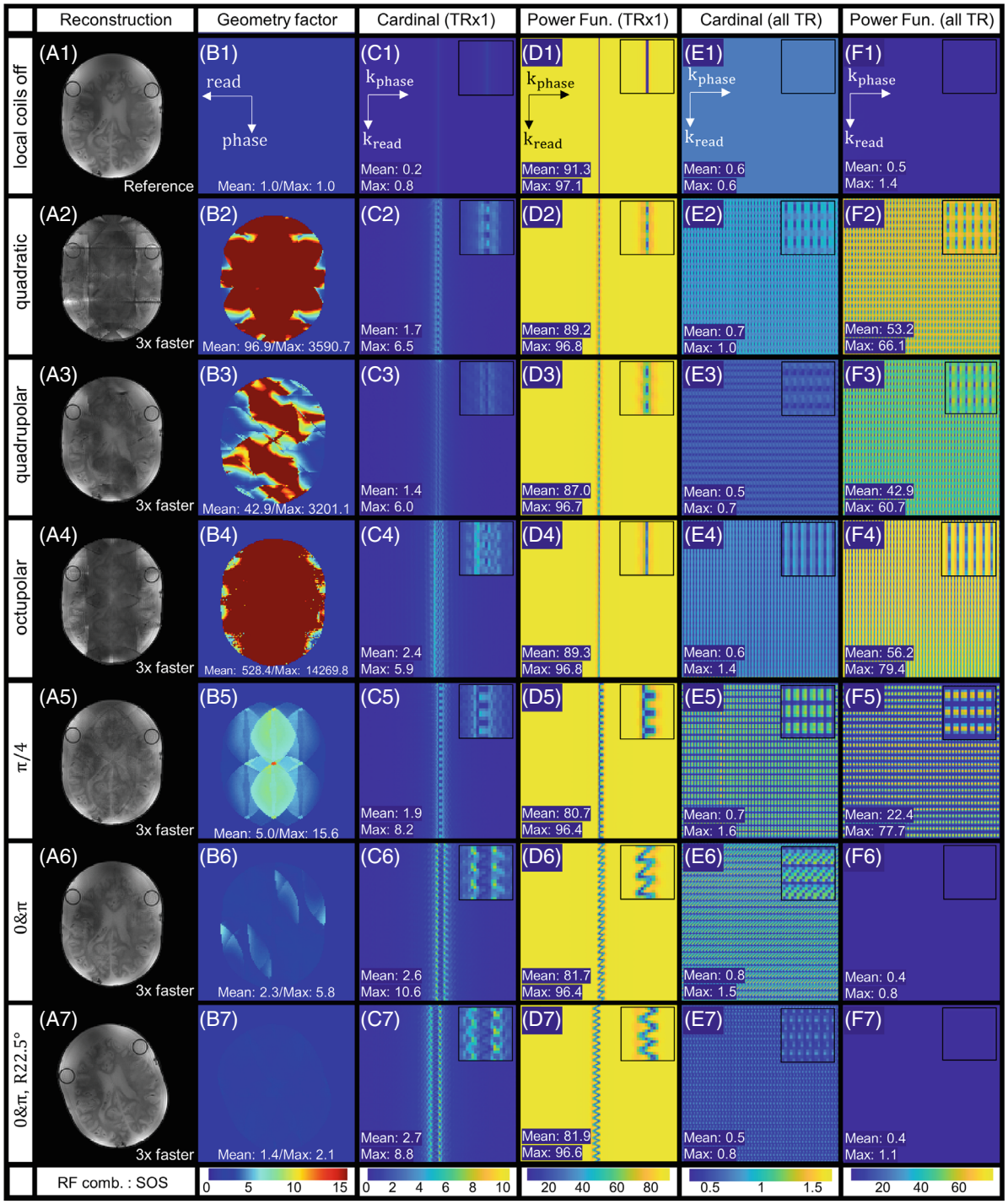

FIGURE 4 Ex vivo scans given local B_0 coils modulations with different sinusoidal phase offset patterns, all with 7 kHz/40A_{pk}. Rows 1–7: The B_0 modulations with different field shapes. Column A to F: reconstruction of a reference and several 3× accelerated FLASH scans by local B_0 coils modulations with RF receiver channels combined using the sum-of-squares method, G-map for noise amplification in image-space, cardinal map for noise amplification in k-space given sampling within one TR, power function map for approximation errors in k-space given sampling within one TR, cardinal map for noise amplification in k-space given sampling overall TR, power function map for approximation errors in k-space given sampling over all TR. The mean and maximum values in columns C and D are calculated from a local region of 20 phase encoding steps around the center of the sampling pattern, and cannot be used to evaluate the overall (i.e., all TR) encoding efficiency for the entire k-space. Note that, the readout and the phase encoding axis in k-space are rotated by 90° relative to image-space, for better visually comparing the k-space coverage widths by different schemes within one TR in a long figure. Additionally, the G-map in B2–B4 contains extremely high values because of the highly unstable inversion of the E^HE term (E: encoding matrix). The reconstruction in A2–A4 computed with the lsqr solver in MATLAB regularizes the solution, but the object texture is severely smoothed out because the signal cannot be recovered regardless of the noise level, corresponding to large mean values of the approximation maps in F2–F4.

15222594, 2024, 2, Downloaded from https://onlinelibrary.wiley.com/doi/10.1002/mrm.29799 by Danish Technical Knowledge, Wiley Online Library on [19/12/2023]. See the Terms and Conditions (https://onlinelibrary.wiley.com/terms-and-conditions) on Wiley Online Library for rules of use; OA articles are governed by the applicable Creative Commons License

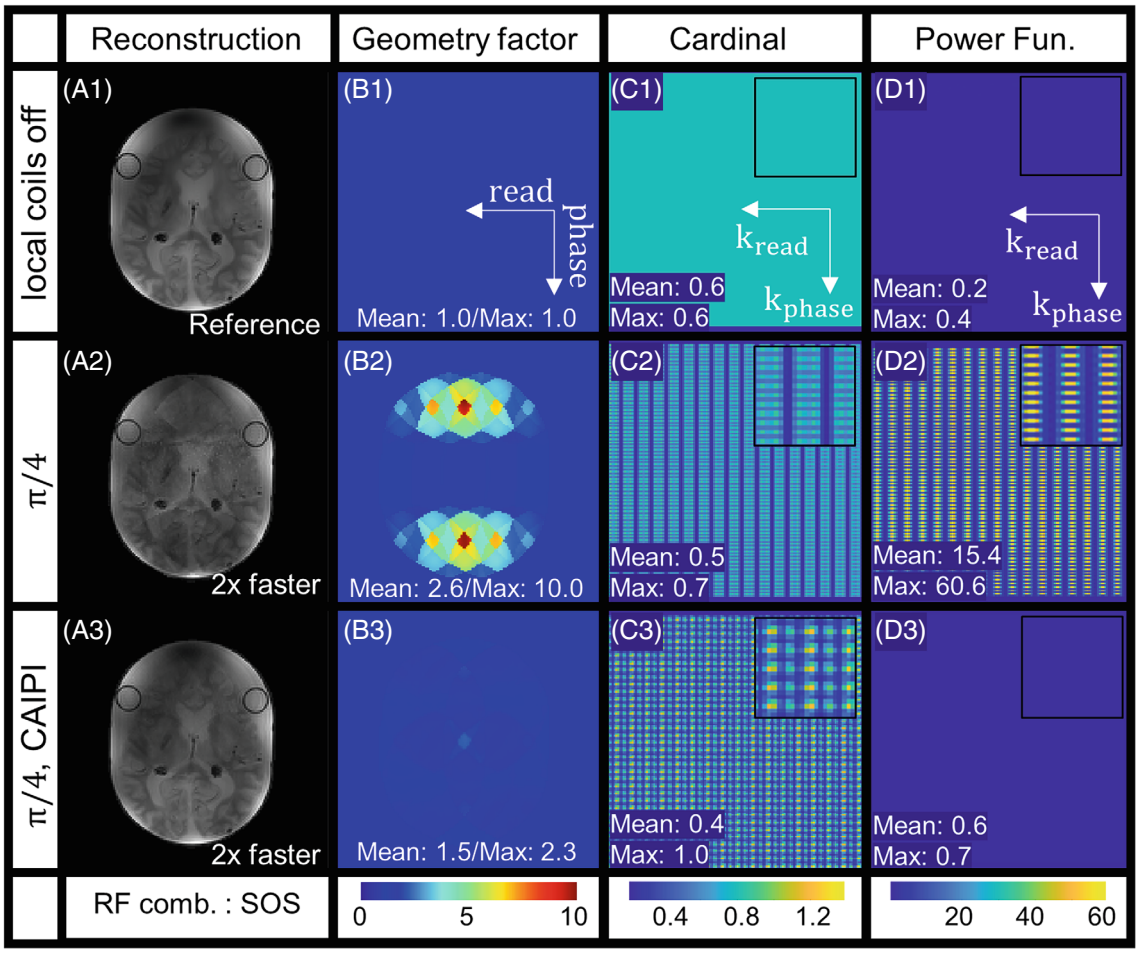

FIGURE 5 Ex vivo scans given 5 kHz/40A_{pk} sinusoidal local B_0 modulation with π shift in all channels between consecutive 2× undersampled phase-encoded steps, manipulating aliasing patterns and mimicking the CAIPIRINHA technique. Rows 1–3: Different modulation schemes—reference fully sampled scan with local coils off, and twofold accelerated FLASH scans with the schemes "π/4" and "π/4, CAIPI", respectively, given all with RF receiver channels combined with the sum-of-squares method. Columns (A)–(D): Reconstructed images, G-map for noise amplification in image-space, cardinal map for noise amplification in k-space, power function map for approximation errors in k-space. Note that, the advantage of applying CAIPI to local B_0 coils here cannot be simply generalized to other scenarios (e.g., a different undersampling factor or field shape, joint acceleration with RF receivers' sensitivity).

low cardinal function values. Furthermore, the approximation error maps given one TR (column D) indicate high sampling efficiency within the sampling "stamp" and high approximation error as moving further away. Note that, for very localized k-space modulation by local B_0 coils, low cardinal- but high power function can simultaneously take place for regions highly under-sampled.

Therefore, for 2D Cartesian scans with undersampling, the missing k-space data can be optimally sampled by simply applying a linear gradient oscillating along the phase encoding dimension, whereas other schemes gained much less efficiency as their k-space modulation regions are not concentrated along the only one undersampled dimension. This explains the origin of the tendency in the G-maps (Figure 4B) and the full k-space error maps (Figure 4E,F). In the latter, the scheme "0&π, R22.5°" shows the most sufficient k-space sampling pattern, whereas others have more "hot spots" in cardinal or power function maps caused by k-space sampling "holes." Additionally, the schemes "quadratic," "quadrupolar," and "octupolar" show relatively low noise amplification, but very high mean values of approximation errors, which may be due to insufficient acquisitions at the undersampled locations given narrower k-space sampling "stamps," similar to maps by Fourier encoding with a phase-encoded step (Figure 4C1,D1). This also matches the instability of matrix inversion shown in the corresponding G-maps (Figure 4B2–B4). Note that, the statistics (i.e., mean and maximum) for columns C and D are computed based on a local region of the central 20 phase-encoded steps and cannot be used to determine the encoding efficiency of the overall k-space.

15222594, 2024, 2, Downloaded from https://onlinelibrary.wiley.com/doi/10.1002/mrm.29799 by Danish Technical Knowledge, Wiley Online Library on [19/12/2023]. See the Terms and Conditions (https://onlinelibrary.wiley.com/terms-and-conditions) on Wiley Online Library for rules of use; OA articles are governed by the applicable Creative Commons License

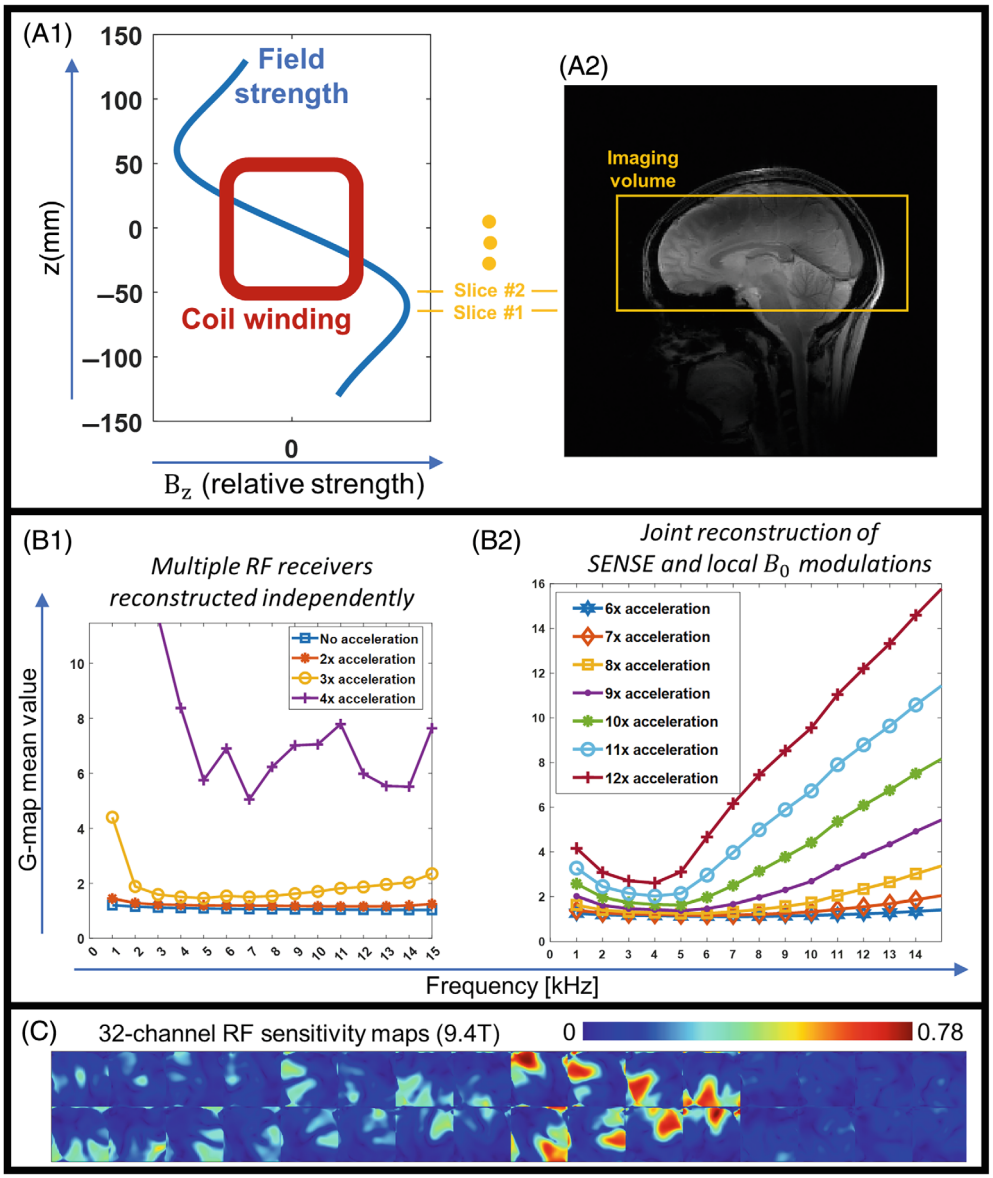

FIGURE 6 Demonstration of the acceleration efficiency for the local B_0 coil array (here, take slice 1 as an example). Row A: The relative position between the human subject and the local B_0 coil array during an in vivo scan. Row B: The noise amplification mean value (image-space) for accelerated scans by local B_0 modulations in different single frequencies, without (B1) and with (B2) joint reconstruction of SENSE, simulated with experimentally measured RF receiver sensitivity maps, field maps of B_0 coils, and sinusoidal currents output by the amplifier. Row C: Measured 32-channel RF receivers' sensitivity maps (magnitude) in 9.4 T with visible "standing wave" patterns. Note that these RF receivers' sensitivity patterns differ from the ones assumed in some nonlinear gradient designs at 3 T, such as PATLOC,[43] O-space,[40] and null space imaging.[74]

4.3 | Sinusoidal modulation with aliasing control

Without combining parallel imaging (i.e., here, SENSE), the phantom scans with (5 kHz/40A_{pk}) sinusoidal phase offsets shift (here, π) in all local B_0 coils between consecutive phase-encoded steps after twofold undersampling are illustrated in Figure 5. As explained in wave-CAIPI,[29] aliasing effects along the readout direction will be induced by the sinusoidal (linear) magnetic field modulations, which together with the aliasing along the phase encoding dimension, are supposed to be resolved during the reconstruction. However, as in Figure 5B2, the "$\pi/4$" scheme with 5 kHz modulation frequency suffers from strong noise amplification, particularly at some "hot spots" reaching G-map value ~10.0. This originates from excessive fold-over of object replicates induced along the readout direction, which can take place when the sinusoidal modulation frequency is too low.

In the local B_0 coil scheme "$\pi/4$, CAIPI", parts of the readout fold-over effects due to 5 kHz field modulation are shifted to the phase encoding direction by varying the phase of sinusoidal currents between phase-encoded steps. This substantially reduces the noise amplification particularly by removing the "hot spots" in G-map, as shown in row 3 of Figure 5. In k-space perspective, given the scheme "$\pi/4$," the power function maps show bright spots as k-space "holes" caused by insufficient sampling. In the "$\pi/4$, CAIPI" scheme, the "hot spots" for approximation errors in k-space are substantially reduced, which indicates more sufficient sampling because of interleaving the shifted "k-space stamps" as in Figure 5C3,D3. However, such CAIPI technique for local B_0 coils might not always lead to significantly improved

15222594, 2024, 2, Downloaded from https://onlinelibrary.wiley.com/doi/10.1002/mrm.29799 by Danish Technical Knowledge, Wiley Online Library on [19/12/2023]. See the Terms and Conditions (https://onlinelibrary.wiley.com/terms-and-conditions) on Wiley Online Library for rules of use; OA articles are governed by the applicable Creative Commons License

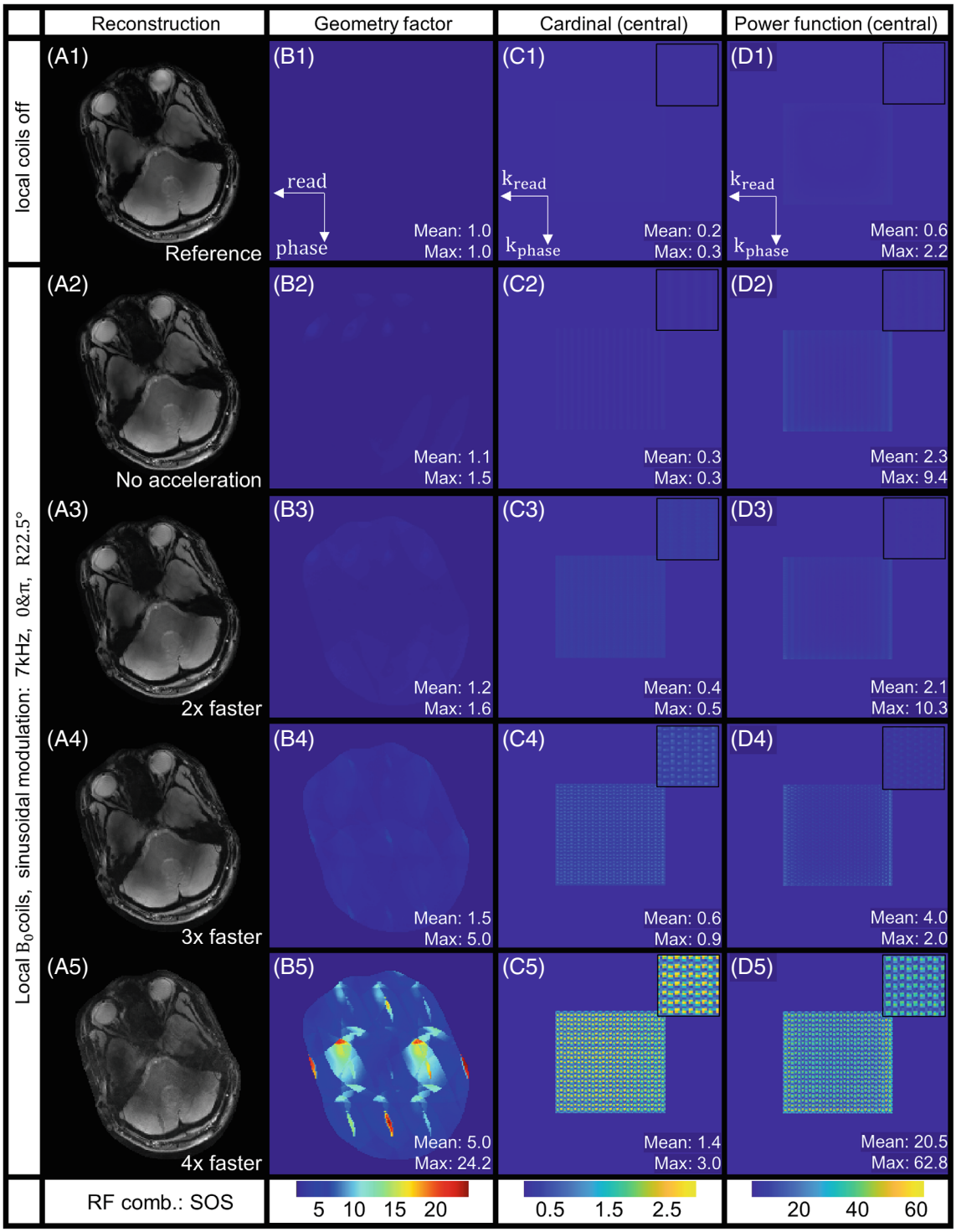

FIGURE 7 Accelerated in vivo FLASH scans with local B_0 coils modulation of 7 kHz/40A_{pk}, given RF receivers' channels combined with the sum-of-squares method. Rows 1–5: A reference scan and several modulated scans with zero to fourfold acceleration. The local coils are modulated with sinusoidal currents with the scheme "0&π, R22.5°." Columns A–D: Reconstructed images, G-map for noise amplification in image-space, cardinal map for noise amplification in k-space, and power function map for approximation error in k-space. Note that only a central region of 86 × 94 pixels was computed for k-space error maps (columns C and D), to avoid excessively demanding computation.

15222594, 2024, 2, Downloaded from https://onlinelibrary.wiley.com/doi/10.1002/mrm.29799 by Danish Technical Knowledge, Wiley Online Library on [19/12/2023]. See the Terms and Conditions (https://onlinelibrary.wiley.com/terms-and-conditions) on Wiley Online Library for rules of use; OA articles are governed by the applicable Creative Commons License

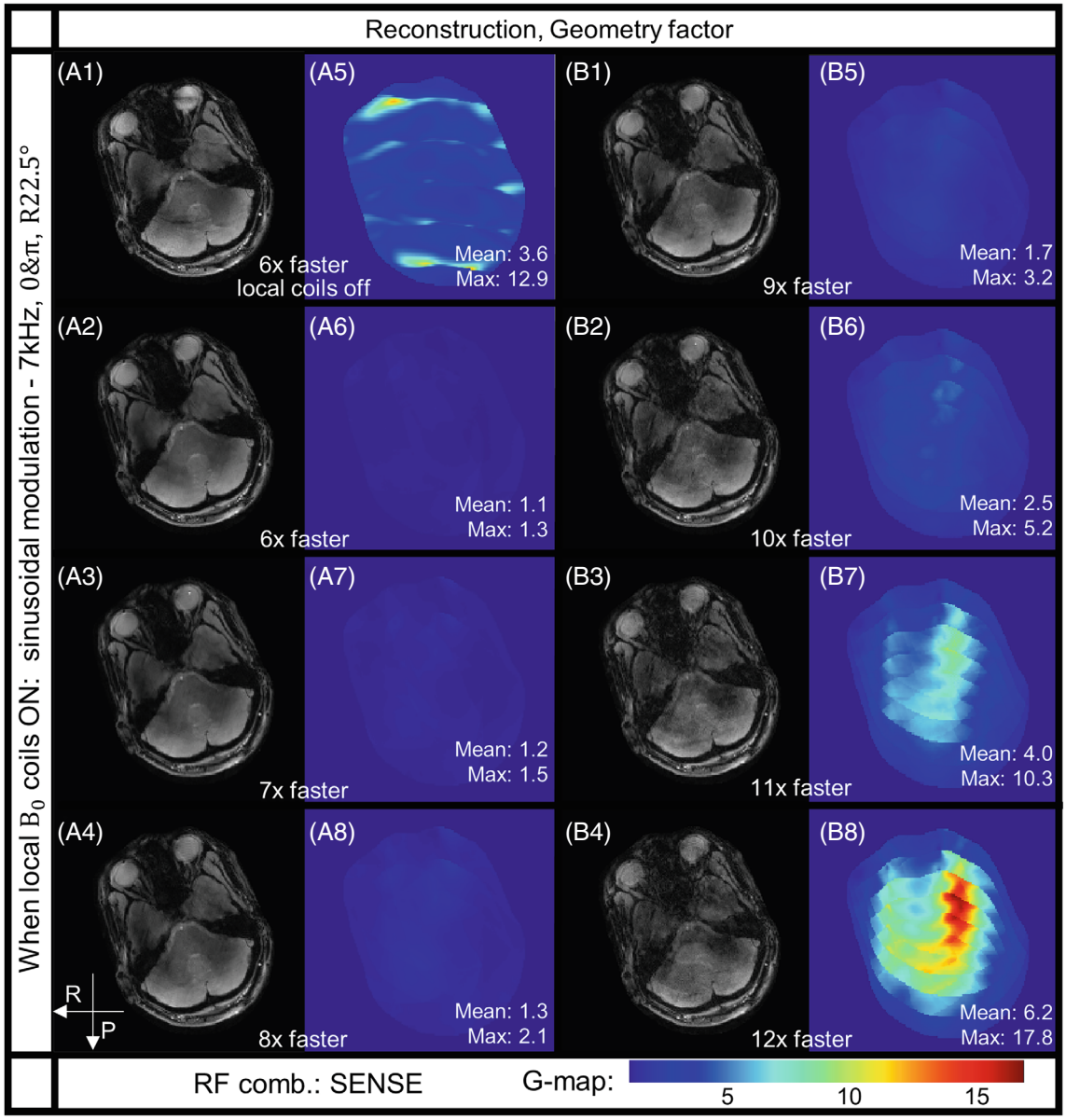

FIGURE 8 In vivo FLASH scans accelerated by sixfold to 12-fold along a phase encoding direction, with joint reconstruction of local coils (7 kHz/40A_{pk}) modulation and SENSE. From A1 to A8: Reconstruction and G-map for accelerated scans ranging from sixfold to eightfold, including a sixfold SENSE reconstruction without local B_0 coils modulation. From B1 to B8: Reconstruction and G-map for accelerated scans from ninefold to 12-fold acceleration factors.

acceleration efficiency in other scenarios, which are shown in Figures S6 and S7.

4.4 | In vivo scans

A safety evaluation of our setup for in vivo scans is performed, which proves our experiments are safe for human subjects with respect to peripheral nerve stimulation and acoustic noise, as documented in Data S1. Therefore, in vivo 2D FLASH scans with local B_0 coil modulations are conducted with healthy volunteers. To maximize encoding efficiency, the "0&π, R22.5°" scheme is used. A pre-scan analysis is demonstrated in Figure 6, including field modulation strength along slice direction, G-map analysis, and the RF receivers' sensitivity pattern as it played an important role in designing other nonlinear gradient methods[39,40,79] (e.g., relying on the 3 T sensitivity distribution to resolve pixels along the circumferential axis, which might be different for 9 T MRI). Here, frequencies with 7, 10, and 13 kHz are applied during in vivo experiments, given potentially milder relaxation induced artifacts as the frequency increases.[29]

As in Figure 7, with the local B_0 coils (7 kHz/40A_{pk}, "0&π, R22.5°") alone, the in vivo 2D FLASH scan is

15222594, 2024, 2, Downloaded from https://onlinelibrary.wiley.com/doi/10.1002/mrm.29799 by Danish Technical Knowledge, Wiley Online Library on [19/12/2023]. See the Terms and Conditions (https://onlinelibrary.wiley.com/terms-and-conditions) on Wiley Online Library for rules of use; OA articles are governed by the applicable Creative Commons License

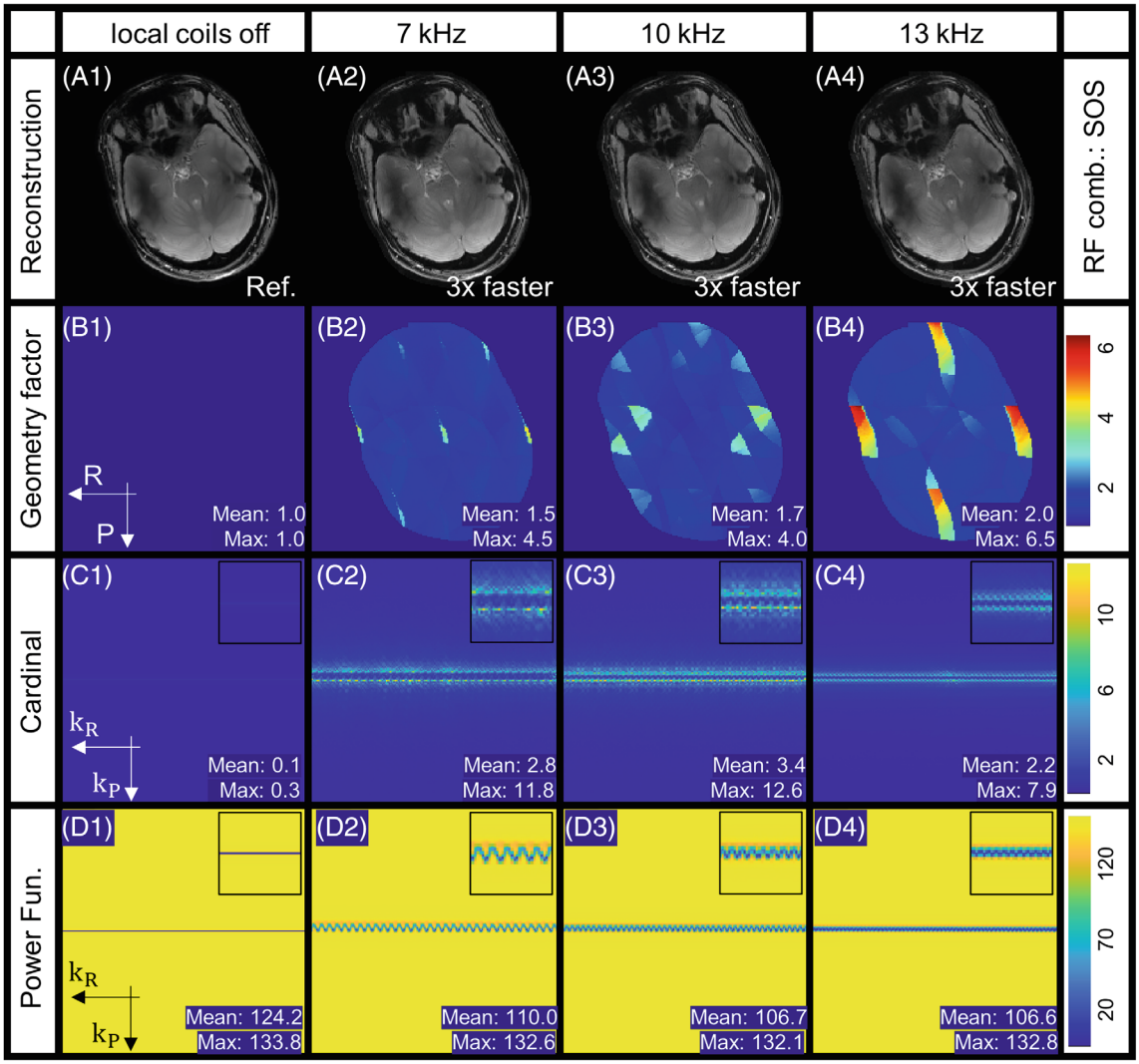

FIGURE 9 In vivo measurement with local B_0 coils modulation, given various modulation frequencies (all in $40A_{pk}$) and multiple RF receivers reconstructed independently. Rows A–D: Reconstructed images, G-map for noise amplification in image-space, cardinal map for noise amplification in k-space, power function map for approximation error in k-space. Columns 1–4: Encoding schemes—reference without local coils, 7, 10, and 13 kHz sinusoidal modulation with the scheme "0&π, R22.5°." The mean and maximum values are calculated from the central 16 phase-encoded steps for encoding.

accelerated by threefold with nearly no visible artifacts, and the G-map mean value remains rather low (i.e., 1.5). When reaching acceleration by a factor of four, "hot spots" in the G-map and the k-space error maps appear, because severe aliasing effects take place in image-space corresponding to insufficient sampling coverage visible in k-space error maps as in Figure 7B5,C5,D5.

As in Figure 8, by joint reconstruction of multiple RF receivers and local B_0 coils modulations, image acceleration along single phase encoding dimension is further enhanced. Compared to the reference scan merely accelerated by SENSE, which shows strong residue artifacts, the accumulative acceleration factor can reach eightfold for 2D Cartesian scan with negligible artifacts. Starting from 10-fold to 11-fold undersampled phase-encoded steps, the artifacts gradually appear protruding, and therefore, the acceleration limit is reached assuming reconstruction in the least squares sense.

Furthermore, the image acceleration with modulation schemes of "0&π, R22.5°" with $40A_{pk}$ in distinct frequencies (7, 10, and 13 kHz) are compared, with multiple RF receivers independently reconstructed (Figure 9) and with joint reconstruction of SENSE and local B_0 modulations (Figure 10), respectively. As in Figure 9, without parallel imaging, the scans accelerated by threefold with modulations in 7 and 10 kHz have negligible artifacts, whereas the one with modulation in 13 kHz has slightly visible errors within very limited support (corresponding to the bottom "bright stripe" in the G-map). From the cardinal and the power function maps given sampling period over one TR,

15222594, 2024, 2, Downloaded from https://onlinelibrary.wiley.com/doi/10.1002/mrm.29799 by Danish Technical Knowledge, Wiley Online Library on [19/12/2023]. See the Terms and Conditions (https://onlinelibrary.wiley.com/terms-and-conditions) on Wiley Online Library for rules of use; OA articles are governed by the applicable Creative Commons License

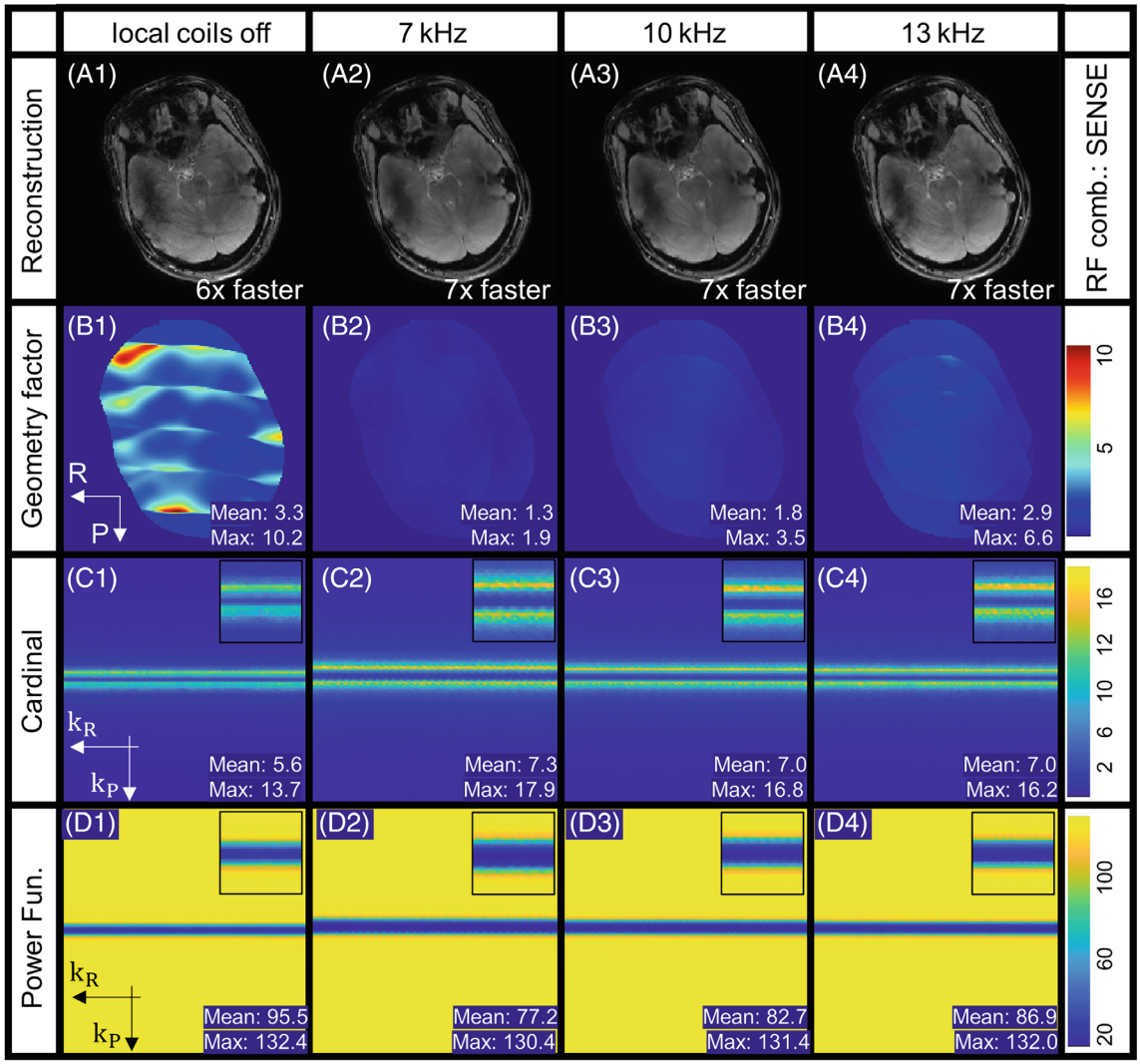

FIGURE 10 In vivo measurement with joint reconstruction of local B_0 coils modulation and SENSE, given various modulation frequencies (all in $40A_{pk}$). Rows A–D: Reconstructed images, G-map for noise amplification in image-space, cardinal map for noise amplification in k-space, power function map for approximation error in k-space. Columns 1–4: Encoding schemes—reference without local coils, 7, 10, and 13 kHz sinusoidal modulation with the scheme "0&π, R22.5°." The mean and maximum values are calculated from the central 24 phase-encoded steps for encoding.

the higher frequency modulation (C4, D4) induces sampling with a narrower k-space "stamp" efficiently resolving data in more localized regions, as indicated by the narrow dark band around the k-space center. The maps for lower frequencies contain wider and brighter regions and imply acquisitions with k-space "stamps" reaching broader range of pixels along the phase encoding dimension, although incapable of resolving all these pixels without more phase-encoded steps, which matches with the prediction by the Eq. (7).

In Figure 10, when combined with SENSE, the 7× accelerated scans (A2–A4) outperformed the 6× accelerated reference reconstruction with the local B_0 coils off. Moreover, the cardinal and power function maps, compared to the ones without SENSE, quantitatively demonstrated the encoding behavior when combining the effects by RF receivers' sensitivity modulation (i.e., GRAPPA kernel)[14] and the dynamic "k-space stamp"[32] because of local B_0 modulations, which generally broadens the zig-zag trajectory by B_0 gradients. The lower frequency modulation (i.e., 7 kHz) leads to a wider dark band in k-space error maps (Figure 10C2,D2) and the least image-space SNR loss (Figure 9B2), which matches the prediction of Eq. (7).

5 | DISCUSSION AND CONCLUSIONS

Our proposed local B_0 coil encoding technique is proved to successfully accelerate 2D Cartesian FLASH scans, given the almost artifacts-free threefold and eightfold

15322594, 2024, 2, Downloaded from https://onlinelibrary.wiley.com/doi/10.1002/mrm.29799 by Danish Technical Knowledge, Wiley Online Library on [19/12/2023]. See the Terms and Conditions (https://onlinelibrary.wiley.com/terms-and-conditions) on Wiley Online Library for rules of use; OA articles are governed by the applicable Creative Commons License

undersampled reconstructions, without and with joint acceleration with SENSE, respectively. The quantitative k-space efficiency maps incorporating nonlinear gradients are analytically computed by the extended MRI sampling theory based on RKHS,[63] and therefore, the encoding behaviors by various nonlinear gradient modulation schemes can be visually compared along their time-domain "trajectory" within arbitrary sampling duration (e.g., entire k-space, a single TR coverage). The optimal 8-channel modulation waveforms for 2D Cartesian scans turn out to produce a nearly linear gradient oscillating along the phase encoding dimension, leading to substantial SNR improvement compared to the previous work.[46] The aliasing control technique appears helpful, although limited within certain scenarios. The encoding effects by sinusoidal modulation with different frequencies, optionally combined with SENSE, can also be visually compared in k-space quantitatively. The proposed field calibration technique, the novel encoding analysis tools, the safety evaluation procedure for our custom-built gradient system, and the demonstrated reconstruction examples for 2D Cartesian scans make significant steps toward pushing MRI speed further with local B_0 coil array.

Notably, pushing the nonlinear B_0 gradient encoding into the RKHS theory not only finds another important application for this mathematical framework beyond parallel imaging,[63] but also provides an example showing how the k-space efficiency maps computed based on a time segment (e.g., a single TR as demonstrated in this paper) can decouple the entire acquisition duration and quantify individual contributions of encoding within smaller temporal periods. This elucidates the origins of the k-space "holes" observed in many nonlinear field modulation schemes explored within this study, and potentially, could be used to formulate the cost functions in optimization programs to search further enhanced encoding strategies, with less computation time and memory requirements compared to evaluating the entire nonlinear field encoding matrix. Moreover, as pointed by Eqs. (2) and (3), the time-domain coverage and sampling efficiency by arbitrary acquisition strategies given linear B_0 gradients and nonlinear B_0/B_1 fields can also be rigorously analyzed and compared in a "quantitative" k-space by applying the RKHS formalism similarly to the present investigation, such as other nonlinear B_0 gradients methods,[36,39,40,43,31] RF encoding techniques with the transmit[64,66–68] and the switching receive fields,[65,69–72] resolution enhanced scans with subpixel spatial modulations within in-plane,[80–85] and along slice dimension,[86] just to name a few.

In this paper, the optimal modulation scheme "0&π, R22.5°" for in vivo scans can be seen as a (nearly) bunched phase encoding with a local B_0 coil setup. Such field modulation becomes similar to the one produced by a local linear gradient insert,[75,76] with higher energy efficiency and less peripheral nerve stimulation thresholds compared to large-sized scanner gradients. With the current geometry, the magnetic field produced by the local B_0 coils varies slowly across the FOV, as governed by the Biot-Savart law, and is still far less localized to independently modulating just groups of a few pixels. Furthermore, more arbitrary (i.e., spatially and temporally) waveforms than the sinusoidal currents, which remain identical or only vary by π between adjacent phase-encoded steps (i.e., CAIPI) in this paper, can be used for the local B_0 array. However, as a few examples shown in Data S1, for accelerated 2D Cartesian scans, seemingly more flexible B_0 modulations do not necessarily enhance the efficiency in the least squares reconstruction. This is because the linear gradient remains the main "encoder" and leaves a pattern of missing k-space data naturally fit by simply a zig-zag trajectory, which is different than the trajectory optimization in PATLOC (i.e., parallel imaging technique using local gradients)[42–44,60–62] and O-space[87] where nonlinear gradients are used for phase and frequency encoding, instead of merely local modulations in k-space.

Nevertheless, our results do not eliminate all possibilities for potential advantages in signal encoding with more arbitrary field modulation, particularly considering scenario beyond 2D Cartesian sampling, such as 3D Cartesian and spiral.[52] However, in non-Cartesian scans with local coils modulation, system errors (e.g., eddy current, time delay) can manifest as much more severe artifacts, which requires further experimental validation. To facilitate modulation schemes for other trajectories, additional penalty term can be included to remove possible artifacts, although fast forward operator[88,89] to achieve efficient iterative reconstruction with arbitrary local coil modulation are currently unavailable. In the future, the local B_0 coil acceleration for 3D Cartesian and other non-Cartesian acquisitions remains highly interesting, with open questions remaining for the optimal encoding methods and the potential engineering difficulties.

ACKNOWLEDGMENTS

This study is supported by the ERC Advanced Grant (No. 834940). The ex vivo brain phantom was with courtesy of the Institute of Clinical Anatomy and Cell Analysis, Department of Anatomy, Eberhard Karls University of Tübingen. The first author thanks Dr. Thomas Shiozawa (Institute of Clinical Anatomy and Cell Analysis) for assistance with sample preparation, and Dr. Gisela Hagberg for assistance in scanning this phantom. The first author also thanks Stefan Plappert for guidance in programming the ADwin high-speed processor, Praveen Iyyappan Valsala for assistance in using the Skope field camera,

15222594, 2024, 2, Downloaded from https://onlinelibrary.wiley.com/doi/10.1002/mrm.29799 by Danish Technical Knowledge, Wiley Online Library on [19/12/2023]. See the Terms and Conditions (https://onlinelibrary.wiley.com/terms-and-conditions) on Wiley Online Library for rules of use; OA articles are governed by the applicable Creative Commons License

Dr. Alexander Loktyushin for discussions about image reconstruction, Felix Glang for proofreading this manuscript and discussions about image reconstruction, and Prof. Jason Stockmann and Dr. Sebastian Littin for interesting discussions about nonlinear gradients. M.D. receives research support from Siemens Healthineers. A.T. was supported by the Lundbeck foundation (grant R313-2019-622). Open Access funding enabled and organized by Projekt DEAL.

CONFLICT OF INTEREST STATEMENT

Dr. Mathias Davids receives research support from Siemens Healthineers.

DATA AVAILABILITY STATEMENT

The source code and experimental data can be available on request.

ORCID

Rui Tian https://orcid.org/0000-0003-0587-1406
Martin Uecker https://orcid.org/0000-0002-8850-809X
Mathias Davids https://orcid.org/0000-0003-0217-9123
Klaus Scheffler https://orcid.org/0000-0001-6316-8773

REFERENCES

1. Lauterbur PC. Image formation by induced local interactions: examples employing nuclear magnetic resonance. *Nature*. 1973;242:190-191. doi:10.1038/242190a0
2. Ljunggren S. A simple graphical representation of Fourier-based imaging methods. *J Magn Reson*. 1983;54:338-343. doi:10.1016/0022-2364(83)90060-4
3. Twieg DB. The *k*-trajectory formulation of the NMR imaging process with applications in analysis and synthesis of imaging methods. *Med Phys*. 1983;10:610-621. doi:10.1118/1.595331
4. Likes RS. Moving gradient zeugmatography US patent document 4,307,343/A/. 1981.
5. IEC-60601-2-33-2022. Edition 4.0. International Electrotechnical Commission. Accessed February 2023. https://webstore.iec.ch/publication/67211
6. Haase A, Frahm J, Matthaei D, Hanicke W, Merboldt K-D. FLASH Imaging. Rapid NMR Imaging Using Low Flip-Angle Pulses. *J Magn Reson*. 1969;67:258-266. doi:10.1016/0022-2364(86)90433-6
7. Mansfield P. Multi-planar image formation using NMR spin echoes. *J Phys C Solid State Phys*. 1977;10:L55-L58. doi:10.1088/0022-3719/10/3/004
8. Stehling MK, Turner R, Mansfield P. Echo-planar imaging: magnetic resonance imaging in a fraction of a second. *Science*. 1991;254:43-50. doi:10.1126/science.1925560
9. Ahn CB, Kim JH, Cho ZH. High-speed spiral-scan Echo planar NMR imaging-I. *IEEE Trans Med Imaging*. 1986;5:2-7. doi:10.1109/TMI.1986.4307732
10. Madore B, Glover GH, Pelc NJ. Unaliasing by fourier-encoding the overlaps using the temporal dimension (UNFOLD), applied to cardiac imaging and fMRI. *Magn Reson Med*. 1999;42:813-828.
11. Roemer PB, Edelstein WA, Hayes CE, Souza SP, Mueller OM. The NMR phased array. *Magn Reson Med*. 1990;16:192-225. doi:10.1002/mrm.1910160203
12. Sodickson DK, Manning WJ. Simultaneous acquisition of spatial harmonics (SMASH): fast imaging with radiofrequency coil arrays. *Magn Reson Med*. 1997;38:591-603. doi:10.1002/mrm.1910380414
13. Pruessmann KP, Weiger M, Scheidegger MB, Boesiger P. SENSE: sensitivity encoding for fast MRI. *Magn Reson Med*. 1999;42:952-962.
14. Griswold MA, Jakob PM, Heidemann RM, et al. Generalized autocalibrating partially parallel acquisitions (GRAPPA). *Magn Reson Med*. 2002;47:1202-1210. doi:10.1002/mrm.10171
15. Larkman DJ, Hajnal JV, Herlihy AH, Coutts GA, Young IR, Ehnholm G. Use of multicoil arrays for separation of signal from multiple slices simultaneously excited. *J Magn Reson Imaging*. 2001;13:313-317.
16. Tsao J, Boesiger P, Pruessmann KP. k-t BLAST and k-t SENSE: dynamic MRI with high frame rate exploiting spatiotemporal correlations. *Magn Reson Med*. 2003;50:1031-1042. doi:10.1002/mrm.10611
17. Moriguchi H, Duerk JL. Bunched phase encoding (BPE): a new fast data acquisition method in MRI. *Magn Reson Med*. 2006;55:633-648. doi:10.1002/mrm.20819
18. Breuer FA, Moriguchi H, Seiberlich N, et al. Zigzag sampling for improved parallel imaging. *Magn Reson Med*. 2008;60:474-478. doi:10.1002/mrm.21643
19. Breuer FA, Blaimer M, Heidemann RM, Mueller MF, Griswold MA, Jakob PM. Controlled aliasing in parallel imaging results in higher acceleration (CAIPIRINHA) for multi-slice imaging. *Magn Reson Med*. 2005;53:684-691. doi:10.1002/mrm.20401
20. Breuer FA, Blaimer M, Mueller MF, et al. Controlled aliasing in volumetric parallel imaging (2D CAIPIRINHA). *Magn Reson Med*. 2006;55:549-556. doi:10.1002/mrm.20787
21. Pruessmann KP, Weiger M, Börnert P, Boesiger P. Advances in sensitivity encoding with arbitrary k-space trajectories. *Magn Reson Med*. 2001;46:638-651. doi:10.1002/mrm.1241
22. Candes EJ, Romberg J, Tao T. Robust uncertainty principles: exact signal reconstruction from highly incomplete frequency information. *IEEE Trans Inf Theory*. 2006;52:489-509. doi:10.1109/TIT.2005.862083
23. Donoho DL. Compressed sensing. *IEEE Trans Inf Theory*. 2006;52:1289-1306. doi:10.1109/TIT.2006.871582
24. Lustig M, Donoho D, Pauly JM. Sparse MRI: the application of compressed sensing for rapid MR imaging. *Magn Reson Med*. 2007;58:1182-1195. doi:10.1002/mrm.21391
25. Gamper U, Boesiger P, Kozerke S. Compressed sensing in dynamic MRI. *Magn Reson Med*. 2008;59:365-373. doi:10.1002/mrm.21477
26. Uecker M, Hohage T, Block KT, Frahm J. Image reconstruction by regularized nonlinear inversion—joint estimation of coil sensitivities and image content. *Magn Reson Med*. 2008;60:674-682. doi:10.1002/mrm.21691
27. Block KT, Uecker M, Frahm J. Model-based iterative reconstruction for radial fast spin-echo MRI. *IEEE Trans Med Imaging*. 2009;28:1759-1769. doi:10.1109/tmi.2009.2023119
28. Block KT, Uecker M, Frahm J. Undersampled radial MRI with multiple coils. Iterative image reconstruction using a total variation constraint. *Magn Reson Med*. 2007;57:1086-1098. doi:10.1002/mrm.21236

15322594, 2024, 2, Downloaded from https://onlinelibrary.wiley.com/doi/10.1002/mrm.29799 by Danish Technical Knowledge, Wiley Online Library on [19/12/2023]. See the Terms and Conditions (https://onlinelibrary.wiley.com/terms-and-conditions) on Wiley Online Library for rules of use; OA articles are governed by the applicable Creative Commons License

29. Bilgic B, Gagoski BA, Cauley SF, et al. Wave-CAIPI for highly accelerated 3D imaging: wave-CAIPI for highly accelerated 3D imaging. *Magn Reson Med*. 2015;73:2152-2162. doi:10.1002/mrm.25347
30. Bilgic B, Ye H, Wald LL, Setsompop K. Simultaneous time interleaved MultiSlice (STIMS) for rapid susceptibility weighted acquisition. *Neuroimage*. 2017;155:577-586. doi:10.1016/j.neuroimage.2017.04.036
31. Wang H, Tam LK, Constable RT, Galiana G. Fast rotary nonlinear spatial acquisition (FRONSAC) imaging. *Magn Reson Med*. 2016;75:1154-1165. doi:10.1002/mrm.25703
32. Galiana G, Stockmann JP, Tam L, Peters D, Tagare H, Constable RT. The role of nonlinear gradients in parallel imaging: a k-space based analysis. *Concepts Magn Reson Part A*. 2012;40A:253-267. doi:10.1002/cmr.a.21243
33. Engel M, Kasper L, Wilm B, et al. T-hex: tilted hexagonal grids for rapid 3D imaging. *Magn Reson Med*. 2021;85:2507-2523. doi:10.1002/mrm.28600
34. Dispenza NL, Littin S, Zaitsev M, Constable RT, Galiana G. Clinical potential of a new approach to MRI acceleration. *Sci Rep*. 2019;9:1912. doi:10.1038/s41598-018-36802-5
35. Yamada Y, Tanaka K, Abe Z. NMR Fresnel transform imaging technique using a quadratic nonlinear field gradient. *Rev Sci Instrum*. 1992;63:5348-5358. doi:10.1063/1.1143401
36. Patz S, Hrovat MI, Pulyer YM, Rybicki FJ. Novel encoding technology for ultrafast MRI in a limited spatial region. *Int J Imaging Syst Technol*. 1999;10:216-224.
37. Rybicki FJ, Patz S, Hrovat MI, Pulyer YM. Reconstruction algorithm for novel ultrafast magnetic resonance imaging. *Int J Imaging Syst Technol*. 1999;10:209-215.
38. Parker DL, Hadley JR. Multiple-region gradient arrays for extended field of view, increased performance, and reduced nerve stimulation in magnetic resonance imaging. *Magn Reson Med*. 2006;56:1251-1260. doi:10.1002/mrm.21063
39. Hennig J, Welz AM, Schultz G, et al. Parallel imaging in non-bijective, curvilinear magnetic field gradients: a concept study. *Magn Reson Mater Phys Biol Med*. 2008;21:5-14. doi:10.1007/s10334-008-0105-7
40. Stockmann JP, Ciris PA, Galiana G, Tam L, Constable RT. *O*-space imaging: highly efficient parallel imaging using second-order nonlinear fields as encoding gradients with no phase encoding. *Magn Reson Med*. 2010;64:447-456. doi:10.1002/mrm.22425
41. Schultz G, Ullmann P, Lehr H, Welz AM, Hennig J, Zaitsev M. Reconstruction of MRI data encoded with arbitrarily shaped, curvilinear, nonbijective magnetic fields. *Magn Reson Med*. 2010;64:1390-1403. doi:10.1002/mrm.22393
42. Schultz G, Weber H, Gallichan D, et al. Radial imaging with multipolar magnetic encoding fields. *IEEE Trans Med Imaging*. 2011;30:2134-2145. doi:10.1109/TMI.2011.2164262
43. Gallichan D, Cocosco CA, Dewdney A, et al. Simultaneously driven linear and nonlinear spatial encoding fields in MRI. *Magn Reson Med*. 2010;65:702-714. doi:10.1002/mrm.22672
44. Witschey WRT, Cocosco CA, Gallichan D, et al. Localization by nonlinear phase preparation and K-space trajectory design. *Magn Reson Med*. 2011;67:1620-1632. doi:10.1002/mrm.23146
45. Layton KJ, Morelande M, Farrell PM, Moran B, Johnston LA. Performance analysis for magnetic resonance imaging with nonlinear encoding fields. *IEEE Trans Med Imaging*. 2012;31:391-404. doi:10.1109/TMI.2011.2169969
46. Scheffler K, Loktyushin A, Bause J, Aghaeifar A, Steffen T, Schölkopf B. Spread-spectrum magnetic resonance imaging. *Magn Reson Med*. 2019;82:877-885. doi:10.1002/mrm.27766
47. Juchem C, Nixon TW, McIntyre S, Boer VO, Rothman DL, de Graaf RA. Dynamic multi-coil shimming of the human brain at 7T. *J Magn Reson*. 2011;212:280-288. doi:10.1016/j.jmr.2011.07.005
48. Aghaeifar A, Zhou J, Heule R, et al. A 32-channel multi-coil setup optimized for human brain shimming at 9.4T. *Magn Reson Med*. 2020;83:749-764. doi:10.1002/mrm.27929
49. Viterbi AJ. *CDMA: Principles of Spread Spectrum Communication*. Addison-Wesley; 2001.
50. Avdievich NI, Giapitzakis IA, Bause J, Shajan G, Scheffler K, Henning A. Double-row 18-loop transceive-32-loop receive tight-fit array provides for whole-brain coverage, high transmit performance, and SNR improvement near the brain center at 9.4T. *Magn Reson Med*. 2019;81:3392-3405. doi:10.1002/mrm.27602
51. Uecker M, Lai P, Murphy MJ, et al. ESPIRiT-an eigenvalue approach to autocalibrating parallel MRI: where SENSE meets GRAPPA. *Magn Reson Med*. 2014;71:990-1001. doi:10.1002/mrm.24751
52. Tian R, Loktyushin A, Buckenmaier K, Steffen T, Scheffler K. Image acceleration with an 8-channel local B_0 coil array compatible with parallel imaging in a 9.4T human MR scanner. *In Proceedings of the Joint Annual Meeting of ISMRM-ESMRMB*. London, UK: ISMRM; 2022. Abstract #0388.
53. Tian R, Davids M, Thielscher A, Buckenmaier K, Steffen T, Scheffler K. Safety evaluation of an 8-channel local B_0 coil array with sinusoidal modulation in a 9.4T human MR scanner. *ISMRM Workshop on MR Safety: from Physics & Physiology to Policies & Practice*. New York, USA: ISMRM; 2022.
54. Tian R, Steffen T, Scheffler K. In-vivo image acceleration with an 8-channel local B coil array and parallel imaging in a 9.4T human MR scanner. *In Proceedings of the Annual Meeting of ISMRM*. Toronto, Canada: ISMRM; 2023. Abstract #4652.
55. Barrett R, Berry M, Chan TF, et al. *Templates for the Solution of Linear Systems: Building Blocks for Iterative Methods*. SIAM; 1994.
56. Paige CC, Saunders MA. LSQR: an algorithm for sparse linear equations and sparse least squares. *ACM Trans Math Softw*. 1982;8:43-71. doi:10.1145/355984.355989
57. Gordon R, Bender R, Herman GT. Algebraic reconstruction techniques (ART) for three-dimensional electron microscopy and X-ray photography. *J Theor Biol*. 1970;29:471-481. doi:10.1016/0022-5193(70)90109-8
58. Kak AC, Slaney M. *Principles of Computerized Tomographic Imaging*. Society for Industrial and Applied Mathematics; 2001. doi:10.1137/1.9780898719277
59. Lin FH, Witzel T, Schultz G, et al. Reconstruction of MRI data encoded by multiple nonbijective curvilinear magnetic fields. *Magn Reson Med*. 2012;68:1145-1156. doi:10.1002/mrm.24115
60. Lin FH. Multidimensionally encoded magnetic resonance imaging. *Magn Reson Med*. 2013;70:86-96. doi:10.1002/mrm.24443
61. Layton KJ, Gallichan D, Testud F, et al. Single shot trajectory design for region-specific imaging using linear and nonlinear magnetic encoding fields. *Magn Reson Med*. 2013;70:684-696. doi:10.1002/mrm.24494
62. Layton KJ, Kroboth S, Jia F, Littin S, Yu H, Zaitsev M. Trajectory optimization based on the signal-to-noise ratio for

15222594, 2024, 2, Downloaded from https://onlinelibrary.wiley.com/doi/10.1002/mrm.29799 by Danish Technical Knowledge, Wiley Online Library on [19/12/2023]. See the Terms and Conditions (https://onlinelibrary.wiley.com/terms-and-conditions) on Wiley Online Library for rules of use; OA articles are governed by the applicable Creative Commons License

spatial encoding with nonlinear encoding fields. *Magn Reson Med*. 2016;76:104-117. doi:10.1002/mrm.25859
63. Athalye V, Lustig M, Uecker M. Parallel magnetic resonance imaging as approximation in a reproducing kernel Hilbert space. *Inverse Probl*. 2015;31:045008. doi:10.1088/0266-5611/31/4/045008
64. Hoult DI. Rotating frame zeugmatography. *J Magn Reson*. 1969;33:183-197. doi:10.1016/0022-2364(79)90202-6
65. Trakic A, Wang H, Weber E, et al. Image reconstructions with the rotating RF coil. *J Magn Reson*. 2009;201:186-198. doi:10.1016/j.jmr.2009.09.009
66. Katscher U, Lisinski J, Börnert P. RF encoding using a multielement parallel transmit system. *Magn Reson Med*. 2010;63:1463-1470. doi:10.1002/mrm.22439
67. Sharp JC, King SB. MRI using radiofrequency magnetic field phase gradients. *Magn Reson Med*. 2010;63:151-161. doi:10.1002/mrm.22188
68. Kartäusch R, Driessle T, Kampf T, et al. Spatial phase encoding exploiting the Bloch–Siegert shift effect. *Magn Reson Mater Phys Biol Med*. 2014;27:363-371. doi:10.1007/s10334-013-0417-0
69. Li M, Jin J, Trakic A, et al. Hign acceleration with a rotating radiofrequency coil array (RRFCA) in parallel magnetic resonance imaging (MRI). *2012 Annual International Conference of the IEEE Engineering in Medicine and Biology Society*. 2012;1098-1101. doi:10.1109/EMBC.2012.6346126
70. Li M, Zuo Z, Jin J, et al. Highly accelerated acquisition and homogeneous image reconstruction with rotating RF coil array at 7T—A phantom based study. *J Magn Reson*. 2014;240:102-112. doi:10.1016/j.jmr.2013.11.002
71. Li M, Weber E, Jin J, et al. Radial magnetic resonance imaging (MRI) using a rotating radiofrequency (RF) coil at 9.4 T. *NMR Biomed*. 2018;31:e3860. doi:10.1002/nbm.3860
72. Glang F, Nikulin AV, Bause J, et al. Accelerated MRI at 9.4 T with electronically modulated time-varying receive sensitivities. *Magn Reson Med*. 2022;88:742-756. doi:10.1002/mrm.29245
73. Levine E, Hargreaves B. On-the-Fly adaptive *k*-space sampling for linear MRI reconstruction using moment-based spectral analysis. *IEEE Trans Med Imaging*. 2018;37:557-567. doi:10.1109/TMI.2017.2766131
74. Weiger M, Overweg J, Rösler MB, et al. A high-performance gradient insert for rapid and short-T2 imaging at full duty cycle. *Magn Reson Med*. 2018;79:3256-3266. doi:10.1002/mrm.26954
75. Versteeg E, Klomp DWJ, Siero JCW. A silent gradient axis for soundless spatial encoding to enable fast and quiet brain imaging. *Magn Reson Med*. 2022;87:1062-1073. doi:10.1002/mrm.29010
76. Versteeg E, Klomp DWJ, Siero JCW. Accelerating brain imaging using a silent spatial encoding Axis. *Magn Reson Med*. 2022;88:1785-1793. doi:10.1002/mrm.29350
77. Wang G, Luo T, Nielsen JF, Noll DC, Fessler JA. B-spline parameterized joint optimization of reconstruction and K-space trajectories (BJORK) for accelerated 2D MRI. *IEEE Trans Med Imaging*. 2022;41:2318-2330. doi:10.1109/TMI.2022.3161875
78. Xu J, Stockmann J, Bilgic B, et al. Multi-frequency wave-encoding (mf-wave) on gradients and multi-coil shim-array hardware for highly accelerated acquisition. *In Proceedings of the Annual Meeting of ISMRM*. 2020; Abstract #0618.
79. Tam LK, Stockmann JP, Galiana G, Constable RT. Null space imaging: nonlinear magnetic encoding fields designed complementary to receiver coil sensitivities for improved acceleration in parallel imaging. *Magn Reson Med*. 2012;68:1166-1175. doi:10.1002/mrm.24114
80. Ropele S, Ebner F, Fazekas F, Reishofer G. Super-resolution MRI using microscopic spatial modulation of magnetization. *Magn Reson Med*. 2010;64:1671-1675. doi:10.1002/mrm.22616
81. Hennel F, Pruessmann KP. MRI with phaseless encoding. *Magn Reson Med*. 2017;78:1029-1037. doi:10.1002/mrm.26497
82. Hennel F, Tian R, Engel M, Pruessmann KP. In-plane "super-resolution" MRI with phaseless sub-pixel encoding. *Magn Reson Med*. 2018;80:2384-2392. doi:10.1002/mrm.27209
83. Tian R, Hennel F, Pruessmann KP. Low-distortion diffusion tensor MRI with improved phaseless encoding. *J Magn Reson*. 2019;309:106602. doi:10.1016/j.jmr.2019.106602
84. Lally PJ, Matthews PM, Bangerter NK. Unbalanced SSFP for super-resolution in MRI. *Magn Reson Med*. 2021;85:2477-2489. doi:10.1002/mrm.28593
85. Tian R, Hennel F, Bianchi S, Pruessmann KP. Superresolution MRI with a structured-illumination approach. *Phys Rev Appl*. 2023;19:034074. doi:10.1103/PhysRevApplied.19.034074
86. Setsompop K, Fan Q, Stockmann J, et al. High-resolution in vivo diffusion imaging of the human brain with generalized slice dithered enhanced resolution: simultaneous multislice (gSlider-SMS). *Magn Reson Med*. 2018;79:141-151. doi:10.1002/mrm.26653
87. Tam LK, Galiana G, Stockmann JP, Tagare H, Peters DC, Constable RT. Pseudo-random center placement O-space imaging for improved incoherence compressed sensing parallel MRI. *Magn Reson Med*. 2015;73:2212-2224. doi:10.1002/mrm.25364
88. Fessler JA. On NUFFT-based gridding for non-cartesian MRI. *J Magn Reson*. 2007;188:191-195. doi:10.1016/j.jmr.2007.06.012
89. Knoll F, Schultz G, Bredies K, et al. Reconstruction of undersampled radial PatLoc imaging using total generalized variation. *Magn Reson Med*. 2013;70:40-52. doi:10.1002/mrm.24426

SUPPORTING INFORMATION

Additional supporting information may be found in the online version of the article at the publisher's website.

Figure S1. Pictures of hardware components of our system for image acceleration. (A) The 9.4 T whole-body human scanner. (B) The 16-transceive-32-receive RF array. (C) The power amplifier. (D) The 8-channel local B_0 coil array. (E) The 8-channel local B_0 coil array during manufacturing. (F) The 8-channel fuse box. (G) The high-speed processor for waveform transmission and current monitor sampling. (H) The 8-channel temperature monitor. (I) The installed setup for in vivo scans with a human subject. (J) The installed setup for field camera measurement of the B_0 field produced by the local coil array.

Figure S2. The joint reconstruction of SENSE and local coils modulation (7 kHz/50A_{pk}, scheme "0&π, R22.5°"), with the B_0 map of each local coil channel extrapolated to the reconstruction resolution with the ESPIRiT algorithm, and a bicubic interpolation technique taking weighted average of 4 x 4 neighboring pixels, respectively.

15222594, 2024, 2, Downloaded from https://onlinelibrary.wiley.com/doi/10.1002/mrm.29799 by Danish Technical Knowledge, Wiley Online Library on [19/12/2023]. See the Terms and Conditions (https://onlinelibrary.wiley.com/terms-and-conditions) on Wiley Online Library for rules of use; OA articles are governed by the applicable Creative Commons License

A: Reference image with the RF channels combined with the sum-of-squares method. No retrospective undersampling is applied. Row B: reconstruction with the high-resolution B_0 map extrapolated by the ESPIRiT algorithm. Row C: reconstruction with the high-resolution B_0 map extrapolated by a bicubic interpolation algorithm ("imresize") in MATLAB. For row B and C, column 1 to 3 correspond to: Joint reconstruction of SENSE and local coils modulation for the retrospective undersampling factor of 6, 7 and 8, respectively.

Figure S3. The error maps by comparing the reference image (Figure S2A) and the joint reconstruction (Figure S2, row B and C) of SENSE and local coils modulation (7 kHz/50A_{pk}, scheme "0&π, R22.5°"). The B_0 map of each local coil channel is extrapolated with the ESPIRiT algorithm, and a bicubic interpolation technique taking weighted average of 4 x 4 neighboring pixels, respectively. Row A: the error images for reconstruction with the field maps extrapolated by ESPIRiT. Row B: the error images for reconstruction with the field maps extrapolated by the bicubic interpolation algorithm. Row C: the SSIM images for reconstruction with the field maps extrapolated by ESPIRiT. Row D: the SSIM images for reconstruction with the field maps extrapolated by the bicubic interpolation algorithm. Column 1 to 3: Joint reconstruction of SENSE and local coils modulation, for retrospective undersampling factor of 6, 7 and 8, respectively. Note that, the RMSE for error images is calculated based on a central window in matrix size of 80 x 60, and the SSIM statistics is made within the object mask.

Figure S4. Safety evaluation of the local B_0 coil array. (A1) Current map simulated in MATLAB. (A2, A3) B field maps simulated with Biot–Savart Law with the current map, given 1A in each coil channel. The net magnetic (B) field (for safety check) and the increased B_z field (for encoding) maps corresponding to a local coil were calculated separately. (A4) The maximal (in-plane) magnetic field distributions along z produced by the local coil array with 50 A in all channels. (A5) The experimentally measured magnetic field (for encoding) map with 50 A in all coils. (A6) The field camera measurements with multiple probe channels, for 50 A (zero to peak) and 1 kHz sinusoidal modulation of all coils with phase offset zero. (A7) The nerve stimulation function for scanner gradients and local coils with 50A_{pk} and 10 kHz sinusoidal modulation. (B1) The PNS threshold calculated by the custom-built software. (B2) The E-field generated by each local coil to predict the magneto-stimulation. (C1) The E-field distribution by each local coil simulated by SimNIBs. (C2) The E-field distribution by linear gradients. (C3) The sum E-field by linearly combining results in C1 and C2. (D) The sound pressure level in *dB* (A) measured by a sound level meter compatible with the 9.4 T scanner. Note that, the E-field calculated by the two software are based on different tissue conductivity, which may be responsible for a different scaling factor.

Table S1. The calculation time in HPC server for cardinal and power functions. R is the acceleration factor. The notation "1 TR" and "150 TR" means k-space error maps covering sampling with 1 and 150 phase-encoded steps respectively. The notation "100 x 100 k-space" means k-space error maps covering only a central region of 100 x 100 pixels, to avoid excessively computation load.

Figure S5. Joint reconstruction with SENSE, for 7 kHz/40A_{pk} sinusoidal modulation with different field shapes. Row 1 to 7: modulation schemes for distinct phase offset patterns of the 8-channel local coils, which forms different field shapes oscillating during signal readout to accelerate scans. Column A to D: reconstructed 2D FLASH images with 8x undersampling, G-map, cardinal map and power function map for sampling period over one TR. In columns C and D, zoomed in pictures are shown on the upper right corner, and the mean and max. values are calculated from the 20 central phase-encoded steps. Note that, the k-space axis is rotated by 90 degree relative to image space, to better visually compare the k-space error maps in a long figure.

Figure S6. Ex vivo scans given 5 kHz/40A_{pk} sinusoidal local coils modulation with π shift in all channels between consecutive two-fold undersampled phase-encoded steps, manipulating aliasing patterns and mimicking the CAIPIRINHA technique. Row 1 to 5: different modulation schemes—reference fully sampled scan with local coils off, and two-fold accelerated FLASH scans with schemes "45°", "45°" with CAIPI, "0&π", "0&π" with CAIPI, respectively, given all with RF receiver channels combined with the sum-of-squares method. Column A to D: reconstructed images, G-map for noise amplification in image space, cardinal map for noise amplification in k-space, power function map for approximation errors in k-space.

Figure S7. More examples for aliasing controls with local coil array. Left column A: The G-maps computed from eight-fold accelerated FLASH scans given 7 kHz/40A_{pk} sinusoidal modulation with two phase offset schemes, with and without CAIPI. Joint reconstruction with SENSE and local coils is performed. Additionally, G-map from a reference scan with only SENSE acceleration is compared. Right column B: G-maps computed from two-fold accelerated FLASH scans with 40A_{pk} sinusoidal modulation, showing 2D aliasing control along readout (R) and phase encoding (R) dimension, by changing the modulation frequency and introducing phase offsets (here, π) between consecutive phase-encoded steps, respectively.

Figure S8. Examples of more temporally and spatially arbitrary B_0 modulations by simulation using the experimental data for Figure 4 (local coils' field maps, phantom

15222594, 2024, 2, Downloaded from https://onlinelibrary.wiley.com/doi/10.1002/mrm.29799 by Danish Technical Knowledge, Wiley Online Library on [19/12/2023]. See the Terms and Conditions (https://onlinelibrary.wiley.com/terms-and-conditions) on Wiley Online Library for rules of use; OA articles are governed by the applicable Creative Commons License

image, all coils with sinusoidal currents up to $40A_{pk}$). Row 1–5: modulation schemes for comparison, consisting of sinusoidal currents with static phase offsets, and those with phase and frequency varying among TR or local B_0 coil channels. Column A to B: the schematics for sinusoidal waveforms in different schemes, the reconstructed images from simulated acquisition data with artificially added noise, the G-map, the Cardinal function, and the power function. In this comparison, no modulation schemes with more variations in currents outperform the one simply with a nearly bunched phase encoding (i.e., row 1, scheme 0&π, identical among TR).

How to cite this article: Tian R, Uecker M, Davids M, et al. Accelerated 2D Cartesian MRI with an 8-channel local B_0 coil array combined with parallel imaging. *Magn Reson Med*. 2024;91:443-465. doi: 10.1002/mrm.29799

15222594, 2024, 2, Downloaded from https://onlinelibrary.wiley.com/doi/10.1002/mrm.29799 by Danish Technical Knowledge, Wiley Online Library on [19/12/2023]. See the Terms and Conditions (https://onlinelibrary.wiley.com/terms-and-conditions) on Wiley Online Library for rules of use; OA articles are governed by the applicable Creative Commons License